REPORT DOCUMENTATION PAGE

Form Approved
OMB No. 0704-0188

Public reporting burden for this collection of information is estimated to average 1 hour per response, including the time for reviewing instructions, searching existing data sources, gathering and maintaining the data needed, and completing and reviewing this collection of information. Send comments regarding this burden estimate or any other aspect of this collection of information, including suggestions for reducing this burden to Department of Defense, Washington Headquarters Services, Directorate for Information Operations and Reports (0704-0188), 1215 Jefferson Davis Highway, Suite 1204, Arlington, VA 22202-4302. Respondents should be aware that notwithstanding any other provision of law, no person shall be subject to any penalty for failing to comply with a collection of information if it does not display a currently valid OMB control number. PLEASE DO NOT RETURN YOUR FORM TO THE ABOVE ADDRESS.

1. REPORT DATE (DD-MM-YYYY)	2. REPORT TYPE	3. DATES COVERED (From - To)
04-10-2004	REPRINT	

4. TITLE AND SUBTITLE
SPECTRAL IRRADIANCE CALIBRATION IN THE INFRARED. XV. ABSOLUTE CALIBRATION OF STANDARD STARS BY EXPERIMENTS ON THE MIDCOURSE SPACE EXPERIMENT

5a. CONTRACT NUMBER

5b. GRANT NUMBER

5c. PROGRAM ELEMENT NUMBER
62601F

6. AUTHOR(S)
S.D. Price, C. Paxson*, C. Engelke**, and T. Murdock*

5d. PROJECT NUMBER
1010

5e. TASK NUMBER
BD

5f. WORK UNIT NUMBER
A1

7. PERFORMING ORGANIZATION NAME(S) AND ADDRESS(ES)

Air Force Research Laboratory
29 Randolph Road
Hanscom AFB MA 01731-3010

8. PERFORMING ORGANIZATION REPORT NUMBER

9. SPONSORING / MONITORING AGENCY NAME(S) AND ADDRESS(ES)

10. SPONSOR/MONITOR'S ACRONYM(S)
AFRL/VSBYB

11. SPONSOR/MONITOR'S REPORT NUMBER(S)
AFRL-VS-TR-2004-1156

12. DISTRIBUTION / AVAILABILITY STATEMENT
Approved for Public Release; Distribution Unlimited

*Frontier Technology, Beverly, MA, **Boston College, Chestnut Hill, MA

13. SUPPLEMENTARY NOTES
REPRINTED FROM: THE ASTRONOMICAL JOURNAL, Vol 128, pp 889-910, August 2004.

14. ABSTRACT

Calibration experiments were conducted with the SPIRIT III infrared instrument on the *Midcourse Space Experiment* (*MSX*) against a number of infrared standard stars and five emissive reference spheres that were ejected at various times during the mission. The physical properties of the 2 cm diameter spheres, such as size and emissivity, were precisely measured in the laboratory. The energy balance equation between the total flux absorbed and that emitted by the sphere is solved to obtain the time-dependent temperature of the sphere under the assumption that the sphere radiates as a blackbody with the measured wavelength-dependent emissivity. The estimated uncertainties in the modeling of the sphere are about 1 K in the thermal component and 3% for the geometric contribution. *MSX* also measured over 150 mean fluxes for eight standard infrared calibration stars during the 10 month mission. The measurements were scaled to the absolute fluxes that Cohen et al. adopt for α CMa (Sirius). The measured spectral energy distributions of the calibration stars relative to Sirius are within the uncertainties that Cohen et al. assign to the absolute fluxes from these stars, with a few exceptions. However, the *MSX* measurement uncertainties are generally much smaller, and the mission-averaged fluxes reveal statistically significant deviations from the Cohen et al. values. Of the calibration stars, only β Peg was found to be variable. *MSX* also measured excess fluxes for α Lyr (Vega) in the 12.1, 14.7, and 21.3 μm spectral bands; the excesses in the latter two bands are consistent with the published thermal model for the dust ring around this star. The absolute calibration of the fluxes of the stellar standards based on the average of the measurements of the spheres over all *MSX* bands and the five experiments agrees with those predicted to within the 1.4% *MSX* measurement uncertainties. The zero-magnitude absolute fluxes proposed by Cohen et al. are validated if the flux from Sirius is increased by 1%.

20041014 002

15. SUBJECT TERMS
Infrared stars
Midcourse space experiment
Instrumentation detectors

16. SECURITY CLASSIFICATION OF:			17. LIMITATION OF ABSTRACT	18. NUMBER OF PAGES	19a. NAME OF RESPONSIBLE PERSON
a. REPORT	b. ABSTRACT	c. THIS PAGE			S. D. Price
UNCLAS	UNCLAS	UNCLAS	SAR	12	19b. TELEPHONE NUMBER (include area code) 781-377-4552

Standard Form 298 (Rev. 8-98)
Prescribed by ANSI Std. 239.18

BEST AVAILABLE COPY

AFRL-VS-HA-TR-2004-1156

THE ASTRONOMICAL JOURNAL, 128:889–910, 2004 August
© 2004. The American Astronomical Society. All rights reserved. Printed in U.S.A.

SPECTRAL IRRADIANCE CALIBRATION IN THE INFRARED. XV. ABSOLUTE CALIBRATION OF STANDARD STARS BY EXPERIMENTS ON THE *MIDCOURSE SPACE EXPERIMENT*

S. D. PRICE,[1] CHARLES PAXSON,[2] CHARLES ENGELKE,[3] AND THOMAS L. MURDOCK[2]
Received 2004 March 29; accepted 2004 April 15

ABSTRACT

Calibration experiments were conducted with the SPIRIT III infrared instrument on the *Midcourse Space Experiment* (*MSX*) against a number of infrared standard stars and five emissive reference spheres that were ejected at various times during the mission. The physical properties of the 2 cm diameter spheres, such as size and emissivity, were precisely measured in the laboratory. The energy balance equation between the total flux absorbed and that emitted by the sphere is solved to obtain the time-dependent temperature of the sphere under the assumption that the sphere radiates as a blackbody with the measured wavelength-dependent emissivity. The estimated uncertainties in the modeling of the sphere are about 1 K in the thermal component and 3% for the geometric contribution. *MSX* also measured over 150 mean fluxes for eight standard infrared calibration stars during the 10 month mission. The measurements were scaled to the absolute fluxes that Cohen et al. adopt for α CMa (Sirius). The measured spectral energy distributions of the calibration stars relative to Sirius are within the uncertainties that Cohen et al. assign to the absolute fluxes from these stars, with a few exceptions. However, the *MSX* measurement uncertainties are generally much smaller, and the mission-averaged fluxes reveal statistically significant deviations from the Cohen et al. values. Of the calibration stars, only β Peg was found to be variable. *MSX* also measured excess fluxes for α Lyr (Vega) in the 12.1, 14.7, and 21.3 μm spectral bands; the excesses in the latter two bands are consistent with the published thermal model for the dust ring around this star. The absolute calibration of the fluxes of the stellar standards based on the average of the measurements of the spheres over all *MSX* bands and the five experiments agrees with those predicted to within the 1.4% *MSX* measurement uncertainties. The zero-magnitude absolute fluxes proposed by Cohen et al. are validated if the flux from Sirius is increased by 1%.

Key words: infrared: stars — instrumentation: detectors

1. INTRODUCTION

The US Department of Defense's *Midcourse Space Experiment* (*MSX*) was designed to obtain ultraviolet through infrared measurements on a wide range of phenomena, including celestial backgrounds. Accurate calibration of the *MSX* sensors was given paramount importance to ensure that the data analysis of the eight separate *MSX* principal investigator (PI) teams had a common calibration pedigree; the eight PI teams were divided by instrument and experimental objectives and conducted diverse experiments that viewed the low background flux of space to the high backgrounds from the hard Earth. Three teams observed man-made objects, three others measured the Earth, atmospheric, and celestial backgrounds, and two others explored technology issues associated with the spacecraft environment and accurately quantifying the performance of the various instruments.

MSX was launched on 1996 April 24 into a ~900 km, nearly Sun-synchronous orbit. The Spatial Infrared Imaging Telescope III (SPIRIT III), the third in a series of relatively large cryogenic spaceborne sensors built by the Space Dynamics Laboratory (SDL) of Utah State University, was the primary instrument during the initial 10 month phase of the mission, which terminated on 1997 February 20 with the depletion of the solid H_2 cryogen. Mill et al. (1994) give an overview of the *MSX* objectives, experiments, and hardware.

SPIRIT III was extensively calibrated on the ground in the SDL Multifunction Infrared Calibrator (MIC-2) and on-orbit. The *MSX* Data Certification and Technology Transfer (DCATT) team provided technical guidance and evaluation of the SPIRIT III ground-based calibrations and was also responsible for creating and executing on-orbit calibration experiments. Approximately three on-orbit stellar calibration experiments were executed each week. The calibration experiments also included absolute flux measurements against five emissive reference spheres that were ejected at various times during the mission. The physical properties of the reference spheres were well measured, and their absolute fluxes were calculated to good precision. The eight reference stars used to calibrate SPIRIT III were chosen from the list of 16 primary and secondary standards created by Cohen et al. (1992a, 1992b, 1995, 1996). Hereafter, the calibration and standards of Cohen and his primary collaborators, Walker and Witteborn, are designated by CWW.

The *MSX* Celestial Backgrounds (CB) team also conducted a calibration experiment against CWW standards and the Cohen et al. (1999) stars that have calibrated spectral templates. These observations provide a semi-independent assessment of the DCATT stellar calibration, as the CB data were taken in a different operating mode of the instrument and were reduced using different procedures. Cohen et al. (2001) described the observations taken by this CB calibration experiment and the procedures they used to reduce the data; as described in a later section, we used an entirely different reduction procedure in the present analysis.

The *MSX* calibration experiments provided precise relative 4.3–21.3 μm photometry with which to assess the scaling between the CWW secondary standard stars with respect to the

[1] Space Vehicles Directorate, Air Force Research Laboratory, 29 Randolph Road, Hanscom AFB, MA 01731; steve.price@hanscom.af.mil.
[2] Frontier Technology, Inc., Suite 450G, 100 Cummings Center, Beverly, MA 01915; CPaxson@bos.fti-net.com, TMurdock@bos.fti-net.com.
[3] Institute for Scientific Research, Boston College, 140 Commonwealth Avenue, Chestnut Hill, MA 02467; Charles.Engelke@hanscom.af.mil.

TABLE 1
SPIRIT III SPECTRAL BANDS

Band	Active Pixels	Isophotal λ_e (μm)	λ at 50% Peak Intensity	Isophotal BW $\Delta\lambda$ (μm)	Zero-Mag. Irradiance (W cm^{-2})	Noise Equivalent Irradiance (W cm^{-2})
A	8 × 192	8.28	6.8–10.8	3.36	8.20×10^{-16}	7×10^{-19}
B_1	2 × 76	4.29	4.22–4.36	0.104	3.28×10^{-16}	1.9×10^{-17}
B_2	2 × 76	4.35	4.24–4.45	0.179	5.36×10^{-16}	1.9×10^{-17}
C	4 × 192	12.13	11.1–13.2	1.72	9.26×10^{-17}	2.3×10^{-18}
D	4 × 192	14.65	13.5–15.9	2.23	5.69×10^{-17}	1.6×10^{-18}
E	2 × 192	21.34	18.2–25.1	6.24	3.56×10^{-17}	7.5×10^{-18}

CWW primary standards, Sirius and Vega, and an absolute calibration of the CWW standards against the emissive reference spheres. The main findings of this analysis are as follows:

1. The precision in the *MSX* measurements is 1% or less for six of the eight stars.
2. Generally, the relative photometry between the CWW primary and secondary standard stars agree to within 1% or less.
3. The calibration star β Peg was rejected from the analysis, as its infrared flux was observed to increase by about 10% during the 8 month period over which it was measured.
4. The averaged biases for stars other than α CMa and the band A bias for α Lyr indicate that the infrared spectral energy distribution for Sirius should be increased by 1%. The *MSX* 12 and 15 μm fluxes for α Lyr are ~4% higher than predicted by CWW, and the 21 μm measurement is ~17% higher.
5. The absolute calibration of the CWW standards by means of the reference spheres is consistent with the absolute fluxes proposed by Cohen et al. (1992a) for the absolute zero-magnitude fluxes for the CWW system.

2. THE *MSX* SPIRIT III TELESCOPE

Mill et al. (1994) and Price et al. (2001) describe the *MSX* spacecraft, the mission, and the SPIRIT III infrared instrument, while Ames & Burt (1993, 1994) provide additional details on the sensor. SPIRIT III was a 35 cm aperture off-axis telescope cooled by a 944 liter solid H_2 cryostat. A Lyot stop, inserted to reduce the sidelobe response from Earth, reduced the clear-aperture collecting area by about 7% to 896 cm^2. The SPIRIT III radiometer had five infrared, line-scanned, blocked impurity band Si:As focal-plane arrays. Each array had eight columns with 192 rows of 18.″3 square detectors. Except for the B bands, the columns covered nearly a 1° cross-scan field. Half the columns were offset by half a pixel row, providing ~9″ sample spacing in the cross-scan direction. The system parameters are presented in Table 1. To reduce the telemetry rate, only half the columns were active, as indicated in the table, but at least one column was active on either side of the stagger. Band B was divided in cross-scan by two different filters centered on the 4.3 μm atmospheric CO_2 band, which reduced the cross-scan field in each of the B bands to 0.°4. Dichroic filters were used to co-align the band A, D, and E arrays in object space and, separately, bands B and C.

Bands B and D are centered on the 4.3 and 15 μm CO_2 atmospheric molecular features, respectively. Band A is the most sensitive and covers a spectral region not easily available from the ground. Band C is a narrower analog of the *Infrared Astronomical Satellite* (*IRAS*) 12 μm filter and band 5 of the *Cosmic Background Explorer* (*COBE*) Diffuse Infrared Background Experiment (DIRBE). Band E is a good analog of DIRBE band 6, which is usually compared with the *IRAS* 25 μm band. The Kurucz model adopted by Cohen et al. (1992a) was used as the source function in deriving the zero-magnitude fluxes listed in the table for each of the radiometer bands.

SPIRIT III had two data acquisition modes and a number of gain states to accommodate the wide range of experimental objectives. An internal scan mirror could sweep the 1° cross-scan field of the focal-plane columns over in-scan amplitudes of 1°, 2°, or 3° at a rate of 0.°46 s^{-1}, or the mirror could be fixed while the spacecraft motion scanned the arrays across the sky at various scan rates. The data were sampled 5 times faster in the mirror-scan mode than in the mirror-fixed mode, nominally at 5 times lower gain and ~2.5 times lower sensitivity. All the DCATT calibration experiments were taken in the mirror-scan mode, while the CB observations used the more sensitive mirror-fixed mode and a 0.°05 s^{-1} spacecraft scan rate. The 12 bit telemetry word provided a dynamic range of about 3000, taking the dark offset into account. The gain is nominally reduced by about a factor of 4 between the four mirror-fixed gain states, which resulted in a total dynamic range of $\sim 2 \times 10^5$. The three gain states in the mirror-scan mode roughly corresponded to the three lowest mirror-fixed gains. Lower gains were used in both the mirror-fixed and mirror-scanned modes to accommodate the large range of fluxes of the stars measured on the calibration experiments.

The mirror-scan noise equivalent irradiances (NEIs) are listed in Table 1, since ~85% of the stellar calibration measurements were taken in this mode; the mirror-fixed NEIs are about 2.5–3 times more sensitive. The NEI changed by about a factor of 4 during the mission because of the increasing noise caused by the rising focal-plane temperature as the solid cryogen was depleted. The mirror-scan calibration observations used all the gain states available, at least in band A, to cover the factor of ~1000 difference between the faintest star (α And) and the brightest (α Ori and CW Leo) measured during these experiments. Whenever possible, the gains were chosen such that the in-band response of the sensor for a given star was on the linear portion of the response curve (<1000 counts per read).

3. THE *MSX* CALIBRATION MEASUREMENTS

The *MSX* calibration rests on three independent legs: a ground characterization in the MIC-2 calibration chamber at SDL, which duplicates the space environment, an on-orbit irradiance calibration against standard stars, and another on-orbit calibration against emissive reference spheres. The ground chamber used a variety of standard sources, all of which are either traceable to National Institute of Standards and Technology (NIST) references or have physical properties precisely measured at the time of calibration; the temperature and spectral

emissivity of the flat-black extended-source plates are an example of the latter.

The radiometric responsivities determined from the ground calibration were initially updated to a point-source irradiance responsivity by a series of early on-orbit calibration measurements against α Boo, assuming the Burdick & Morris (1997) *MSX* in-band fluxes for this star. Observations of four other Cohen et al. (1992b, 1995) standards (α Lyr, α CMa, α Tau, and β Gem) were then used to independently assess the SPIRIT III calibration against α Boo.

3.1. *Ground Calibration*

Garlick et al. (1996) modeled the radiometric response of the SPIRIT III sensor as a series of transfer functions that convert telemetry counts into a linear instrument response,

$$r'_d(t) = B_{i,d}(t)\left[\frac{g_{i,a}(T)L_{i,a}(r_d(t) - D_{i,d}(t), T)}{R_{a,d}G(T)F_{a,d,m}N_{i,d}}\right] \quad (1)$$

with the following definitions:

$r'_d(t)$	Corrected radiometer response for detector d as a function of time t on the same unitless scale as the radiometer output.
$r_d(t)$	Radiometer data in telemetry counts.
$B_{i,d}(t)$	Operator for integration mode i that labels a pixel as bad or anomalous. A bad-pixel designation eliminates data from that detector for the entire observation, called a data collection event or DCE. Fewer than 2% of the detectors were inoperative, besides the 36 that were blocked by the band B filter mask. The anomalous-pixel designation rejects the data from detector d for specific time intervals. "Not a number" (NaN) was substituted for the rejected data for the CB observations; an average of the surrounding data was substituted in the mirror-scanned observations.
$g_{i,a}(T)$	Gain normalization for array a as a function of focal-plane temperature T.
$L_{i,d}(\ldots)$	Correction for the nonlinear response of the detectors (Larsen & Sargent 1997).
$D_{i,d}$	Dark offset.
$R_{a,d}(t)$	Correction for time-related response trends in detector d of array a (Larsen et al. 1998b).
$G_a(T)$	Temperature-dependent response in array a (Sargent 1997).
$F_{a,d,m}$	Correction for response changes over the field of regard as a function of mirror position m.
$N_{i,d}$	Nonuniformity response correction (flat-fielding).

Garlick et al. (1996) also provide analytic expressions for each of the components in equation (1), while considerably more detail is available in the reference listed for a particular component.

The ground calibration uniquely provided quantitative information on a large number of sensor performance parameters (Thurgood et al. 1998).[4] These include

1. Correction for the response as a function of focal-plane temperature;
2. Scale factors between integration modes as a function of temperature;
3. Uniformity correction (flat-fielding) over the field of regard as a function of temperature;
4. Noise model; and
5. Spectral response, both within the filter bandpass and out of band.

With the exception of the nonlinearity correction and the noise model, all the remaining corrections can be, and were, determined without reference to the absolute radiance of the source.

The radiance is obtained by dividing the corrected counts from equation (1) by a single responsivity value for each spectral band:

$$L_{d,t} = r'_d(t)/\mathcal{R}_a, \quad (2)$$

where $L_{d(t)}$ is the measured radiance in W cm^{-2} sr^{-1} for detector d and $\mathcal{R}_a$ is the responsivity in counts per W cm^{-2} sr^{-1} for array a.

The responsivity $\mathcal{R}_a$ in equation (2) was determined from the ground-based calibration by measuring the instrument response to a known radiance from the extended calibration source in the chamber. The irradiance response was obtained by dividing the radiance response by the solid angle of the point-response function in each band:

$$E_a^{-1} = \frac{\Omega_{\mathrm{EFOV}}}{\mathcal{R}_a}P(r'_d(t), \mathrm{PRF}_a). \quad (3)$$

E_a is the irradiance response in band a. The effective beam size Ω_{EFOV} was initially estimated from the ground calibration measurements and included scattering within the filters. P is the point-response function (PRF) operator used to extract photometry on the point source. The somewhat cross-scan–dependent PRFs derived by Mazuk & Lillo (1998) were used to obtain the PRF-fitted photometry for version 2.3 of the *MSX* Point Source Catalog (Egan et al. 2003).

The Radiometer Instrument Products (RIPs) contain the parameters for the various functions in equation (1) and the responsivities in equation (2). The SPIRIT III performance assessment team determined the RIPs from the preflight and on-orbit calibration. RIP files were released episodically during, and after, the mission as knowledge of the behavior of the instrument improved. The final version of the RIPs was used in the present analyses. Products, such as the dark offsets and anomaly files, were determined uniquely for each DCE.

3.2. *On-Orbit Calibration Experiments*

The DCATT team created five experiments to calibrate the SPIRIT III sensor. Stellar standards were measured on all five experiments, including the reference-sphere experiment. The single CB calibration experiment transferred the absolute calibration of primary and secondary CWW standard stars to a number of stars with spectral templates in the Cohen et al. (1999) calibration network.

Each *MSX* DCE is uniquely labeled. The initial two letters in the label identify the PI team responsible for the experiment, DC for DCATT and CB for Celestial Backgrounds. The following four numbers define the exact observing profile for the measurement: the first two digits are the number assigned to the type of experiment executed, while the next two digits specify the subclass of observation within the experiment; the subclass is either a distinct measurement or a specific

[4] This and other cited papers from the Infrared Radiometric Sensor Calibration symposia are available from the Space Dynamics Laboratory of Utah State University.

TABLE 2

STELLAR STANDARDS MEASURED BY *MSX*

Star	Sp. Type	Band A	Band B_1	Band B_2	Band C	Band D	Band E	Obs.
α CMa	A1 V	2.833×10^{-15}	1.146×10^{-15}	1.874×10^{-15}	3.195×10^{-16}	1.959×10^{-16}	1.22×10^{-16}	35/9
α Tau	K5$^+$ III	1.308×10^{-14}	4.628×10^{-15}	7.373×10^{-15}	1.570×10^{-15}	9.529×10^{-16}	6.046×10^{-16}	30/3
α Boo	K1.5 III	1.463×10^{-14}	5.566×10^{-15}	8.813×10^{-15}	1.735×10^{-15}	1.059×10^{-15}	6.744×10^{-16}	25/7
α Lyr	A0 V	8.196×10^{-16}	3.279×10^{-16}	5.364×10^{-16}	9.259×10^{-17}	5.686×10^{-17}	3.555×10^{-17}	19/2
β Gem	K0 III	2.498×10^{-15}	9.759×10^{-16}	1.576×10^{-15}	2.858×10^{-16}	1.762×10^{-16}	1.098×10^{-16}	15/1
β Peg	M2.5 II–III	7.516×10^{-15}	2.722×10^{-15}	4.365×10^{-15}	9.173×10^{-16}	5.711×10^{-16}	3.596×10^{-16}	14/1
γ Cru	M3.4 III	1.827×10^{-14}	6.235×10^{-15}	9.817×10^{-15}	2.224×10^{-15}	1.359×10^{-15}	8.565×10^{-16}	3/1
γ Dra	K5 III	3.111×10^{-15}	1.080×10^{-15}	1.722×10^{-15}	3.729×10^{-16}	2.281×10^{-15}	1.427×10^{-16}	2/1
β And	M0 III	5.391×10^{-15}	1.981×10^{-15}	3.153×10^{-15}	6.494×10^{-16}	3.987×10^{-16}	2.496×10^{-16}	0*/1

NOTES.—Irradiance units are watts per square centimeter. The format of the last column is *a*/*b*, where *a* is number of DC observations and *b* is the CB06 observations; β And has no DC observations because of a transcription error that resulted in observations of α And instead.

measurement geometry within an experiment. Thus, the experiment designations DC2201 through DC2205 denote that these are the DCATT (DC) DCEs defined in the 22nd DCATT experiment plan, which was designed to measure the references spheres 1–5 (01–05). To this is appended a five-digit number assigned to a specific observation. Thus, DC430100018 is the 18th DCE of the DCATT Source Transfer Experiment (DC43) with observing parameters specified under the first subexperiment plan. Only the PI team and experiment number are necessary for the present analysis; however, Cohen et al. (2001) did use the entire designator.

3.3. *Stellar Calibration Measurements*

The nine CWW stellar standards that were measured during the *MSX* calibration experiments are listed in Table 2. The star name is in the first column, its spectral type is given in the next column, and the in-band irradiances are listed in the next six columns. The in-band fluxes are those used by Cohen et al. (2001) for their CB06 analysis, with the γ Cru values being updated during the CB06 analysis. Because of updates in the normalized filter response functions and improved composite spectra, these irradiances differ somewhat from those of Burdick & Morris (1997) that were used in the initial SPIRIT III calibration. The last column in the table lists the number of individual stellar observations—those from the DC experiments listed first and those observed on the CB06's given after the slash. The asterisk on the β And entry notes the fact that α And was measured four times instead, as a result of a transcription error.

Approximately 88% of the DCATT stellar observations were obtained on two of the five DC calibration experiments: the DC43 Source Transfer Experiment and the DC44 benchmark DCEs. Nominally, each star was measured 80 times within a given DCE, although the number of measurements was different for a small number of DCEs. All DCEs were preceded and followed by an internal calibration that measured the instrument response to an internal stimulator at three flux levels and dark offsets in each gain state.

3.3.1. *DC44: Stellar Benchmark Experiment*

This was the standard weekly calibration experiment executed by the program. The experiment was designed to measure two stars on the same DCE. A stellar measurement with the geometry shown in Figure 1 was performed on the first star.

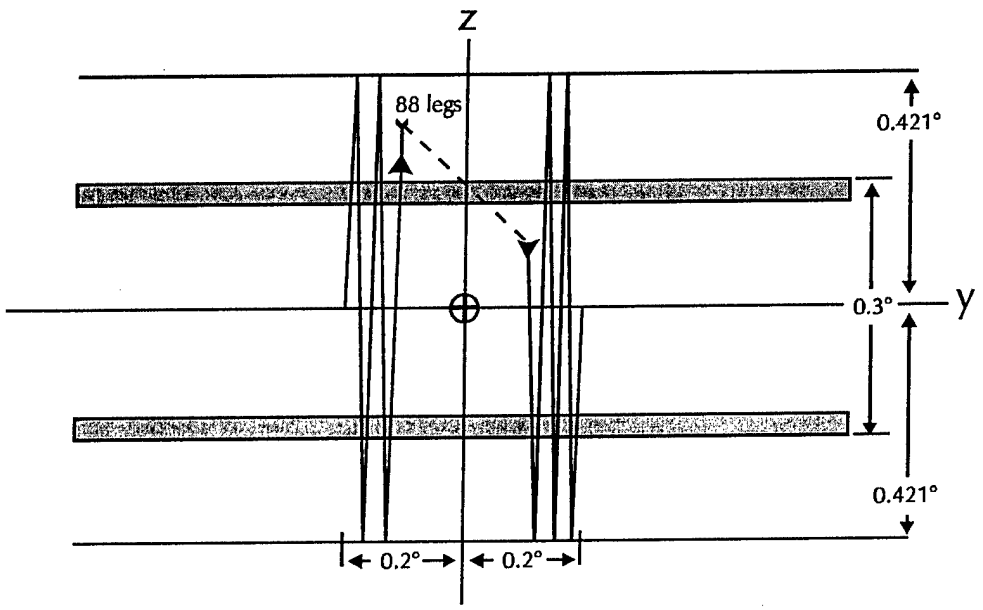

FIG. 1.—Scan geometry used for the DC43 and DC44 DCEs. The spacecraft moves the stars over the central 0°.4 in cross-scan while the mirror is scanning with ~1° amplitude. The gray rectangles represent the fields of view of the co-aligned band A, D, and E arrays and the band B and C arrays.

The spacecraft moved the star 0.°4 in the cross-scan direction, that is, down the focal-plane array columns, while the 1° amplitude mirror scan swept the star back and forth across the arrays; the cross-scan traverse was centered on the center of the *MSX* arrays. The shutter-closed detector dark offsets were measured while SPIRIT III was slewed to a second star. About half the DCEs measured two of the CWW stars listed in Table 2; the other half measured a CWW star and a bright infrared star such as α Ori or CW Leo. Measurements on these bright stars probed the full dynamic range of the sensor and the "wings" of the point-response function. A total of 53 DC44 DCEs were executed, producing 101 observations on stars in Table 2; each of these observations had a nominal 80 measurements on a single DCE.

3.3.2. *DC43: Source Transfer Experiment*

This experiment usually compared two of the stellar calibration standards in Table 2 on the same DCE. The experiment profile was essentially that of DC44, the exception being that a long internal stimulator sequence followed by 5 minutes of measuring the dark offset recovery replaced the DC44 dark offset measurement between the two stellar observations. The stimulator sequence warms the focal plane slightly, and the recovery time allows the dark offset to stabilize. The observing geometry in Figure 1 was also used on this experiment. Forty-eight stellar observations consisting of 80 individual measurements were made on the 25 DC43 DCEs that were executed during the mission.

3.3.3. *DC35: SPIRIT III Radiometric Calibration*

The radiometric responses for each detector in each SPIRIT III spectral band were calibrated against stellar standards under this experiment. As for the DC43 and DC44's, the spacecraft slowly scanned a star in the cross-scan direction down the center of the field of regard using the 1° mirror-scan amplitude. The difference is that the entire 1° cross-scan extent of the array was covered on this experiment and that the $\sim$0.°0002 s^{-1} cross-scan velocity was slow enough to ensure that each detector in the arrays observed the star. Only two sets of observations, one on α Her and the other on α CMa, were made on this experiment, but each star had over 220 individual measurements.

3.3.4. *DC33: Flat-Field Calibration, Mirror-Scan Mode*

This experiment measured the variations in the detector-to-detector responses in each of the SPIRIT III infrared arrays over the entire $1° \times 3°$ field of regard. The SPIRIT III point-response functions, the scan mirror transfer function, and the radiometric calibrations of the arrays were derived from these measurements. A single star was observed on each of the nine DC33 DCEs, and the number of individual stellar measurements on each DCE varied from about 20 to 180.

Two sets of experiment plans were used. For half the DCEs, the spacecraft slowly moved the star along the cross-scan center of the 3° in-scan field of regard swept out by the arrays in the mirror-scan mode. For the remainder of the DCEs, the spacecraft executed a sawtooth pattern with ten 1° cross-scan traverses, while moving across the entire 3° in-scan field of regard. Larsen et al. (1998a) derived the distortion map for the $1° \times 3°$ field scanned by the mirror from the DC33 and DC35 observations. Their Figure 4 shows how these two experiments sampled the response at a number of in-scan and cross-scan positions in the $1° \times 3°$ field of regard.

3.3.5. *CB06: Celestial Radiometric Standards*

Cohen et al. (2001) described this experiment in detail. Briefly, three stars were observed on each DCE with the mirror fixed while the spacecraft scanned the star back and forth across the focal-plane arrays. Nominally, 10 scans were executed at a cross-scan position centered on the band B_1 array, and another 10 centered on the band B_2 array; the scans were at half the cross-scan distance from the center of the *MSX* 1° arrays to their edges. A total of 24 of these DCEs were executed; each DCE obtained 19 or 20 mid-infrared measurements on three stars. Twenty-six observations were obtained on the stars in Table 2, and each star was measured at least once.

3.4. *Emissive Reference Spheres Experiment: DC22*

MSX deployed five emissive reference spheres (ERSs) during the cryogenic lifetime of the SPIRIT III sensor. The ERSs were 1.00 ± 0.01 cm in radius and made of solid 6061-T6 aluminum alloy, which was coated with a Martin Black finish. Thus, the spheres approximated blackbodies with accurately known thermal properties from which instantaneous temperatures could be calculated. The point-source irradiance calibration of the SPIRIT III sensor is derived from the temperature and range of a sphere. The spheres were observed for about a third of an orbital period after ejection. At least one calibration star was also measured on each ERS DCE. Thus, the emissive reference spheres provide calibration of the absolute irradiance responsivity of the mid-infrared bands of the SPIRIT III radiometer and, consequently, the mission-averaged fluxes for the calibration stars, as well as direct calibration of the standard stars measured on the same ERS DCEs.

Nominally, a sphere was deployed forward in the plane of the *MSX* orbit at an elevation angle of 15° and a velocity of 14.2 m s^{-1}. Orbital dynamics accelerated the sphere away from and above the spacecraft after release. The sphere passed through the spacecraft zenith at $t + \sim$1200 s ($\sim$1200 s after release of the sphere) and reached a range of about 67 km at an elevation angle of approximately 41° behind the spacecraft vector when the experiments terminated, at $t + \sim$2200 s. The spacecraft was programmed to track and center the sphere in the $1° \times 3°$ SPIRIT III field of regard. The duration of the DCE was limited by the capacity of the tape recorders and the signal-to-noise ratio of the observations at the end of the DCE. The SPIRIT III measurements were obtained in the highest mirror-scan gain, since the irradiance of the sphere spanned a dynamic range of only $\sim$20 during the measurement period, reaching a signal-to-noise ratio (S/N) of $\sim$10 at the end of the DCE in all radiometer bands.

The detailed timeline for the ERS measurements varied from DCE to DCE. Nominally, stellar observations of 80 measurements each were obtained 14.5 and 7 minutes before the reference sphere was ejected and a final stellar observation was obtained at the end of the DCE, some 45–60 minutes later. A total of 11 stellar observations were obtained on the five ERS DCEs; the initial two stellar measurements are missing on the ERS2 and ERS3 DCEs. Continuous measurements on ERS1 and nearly continuous measurements on ERS5 were obtained from $t + \sim$550 s until $t + \sim$2200 s, the end of the DCE, with dark offset measurements obtained at about 3 minute intervals. Data are missing for portions of the ERS 2, ERS3, and ERS4 for a variety of reasons. An anomalous deployment angle for ERS4 carried the sphere outside the SPIRIT III field of regard until about $t + 1000$ s. The

sensor was also turned off during the South Atlantic Anomaly passage for ERS3 between $t \sim 1250$ and $t \sim 2150$; a similar gap appears for ERS4.

4. DATA PROCESSING

The X-band telemetry from *MSX* was sent to the Applied Physics Laboratory (APL) of Johns Hopkins University in Columbia, Maryland, where it was recorded as Level 0 data on analog tape. These analog tapes were decommutated and formatted into computer-compatible tapes (Level 1 data). The Level 1 data were stripped out for each *MSX* instrument and ordered in increasing time to create Level 1A tapes, which were then sent concurrently to the SPIRIT III Data Processing Center (DPC) at SDL and the Data Analysis Center (DAC) in the Air Force Research Laboratory (VSB/AFRL).

APL also processed the gyroscope and star-tracker information from the spacecraft with the spacecraft ephemeris and the boresight offsets between the various instruments and the spacecraft attitude reference system to create a pointing time history for each DCE. The resulting Definitive Attitude File describes the pointing evolution in J2000 inertial equatorial coordinates corrected for annual and spacecraft aberration. These files were also sent to the SDL DPC and the VSB DAC.

SDL had the responsibility for calibrating the instrument and creating the software that applies this calibration in order to ensure that the results from all the PI teams have a common calibration pedigree. The software, designated Standard CONVERT, is an automated process that converts Level 1A data by means of equation (1) into linear, dark-offset–subtracted and flat-fielded Level 2 data. This software was provided to the data centers supporting each PI team.

The DPC pipeline processing assesses the data quality of each DCE. It strips out housekeeping information, the dark current observations, and the internal stimulator sequences. The mean dark offsets are calculated for each pixel, and the results form a dark offset matrix for each dark measurement. The amplitudes of the stimulator flashes are extracted and used in long-term trending of the sensor response (Larsen et al. 1998b). The pipeline also flags anomalies such as glitches, dropouts, and saturated pixels. The first four standard statistical parameters (mean, standard deviation, skew, and kurtosis) of each pixel are calculated in blocks of 2400 minor frames (6.6 s). The pipeline processing parses the data into blocks this size because it is the volume of data generated during the maximum 3° field of regard swept out by the internal scan mirror.

4.1. *Identification and Photometry of Point Sources in the Mirror-Scan Mode*

Larsen et al. (1996) describe the Canonical CONVERT processing, which identifies point sources in the mirror-scan mode and extracts their irradiances (SDL did not create an equivalent canonical CONVERT routine for the mirror-fixed mode). Succinctly, the steps are as follows.

The data are parsed into scenes 2400 samples in length for each detector, the mirror-scan monitor marks when the mirror reverses direction, and that information defines the beginning of the scene. If necessary, the scene is subdivided into smaller data blocks that correspond to smaller amplitude mirror scans. The Level 2A SPIRIT III radiances were combined with pointing CONVERT to create time- and position-tagged radiances for each detector within the scene; the result was then formed into a quasi image in focal-plane coordinates for source extraction and photometry.

Moving averages and standard deviations were calculated for each detector within the scene. Detector radiances that were greater than an S/N threshold were extracted as part of a potential source, and those that were less than the S/N threshold were incorporated into the background. Background values were interpolated and substituted for the data in the gaps left by values exceeding the threshold criterion. The resulting background data were then smoothed.

The sources consisted of clusters of radiances that exceed an S/N threshold of 10 above the local smoothed background, all of which fell within a radius typical of point sources. The size of a point source was assumed to have a radius of 270 μrad, or three detectors. The total intensity and intensity squared, the in-scan and cross-scan centroids, and in-scan and cross-scan second moments were calculated for the isolated clusters of radiances. These quantities were used to ascertain how round or pointlike the object was, as well as providing an initial estimate of position and intensity. Criteria for these statistics were adopted, and clusters of data values that met or exceeded these criteria were flagged as potential point sources. The amplitude, or flux, and position of the potential source were then simultaneously solved for by minimizing the mean square error between the data and point-response function.

Thus, a detection was deemed to be real if it passed a two-tier selection criterion: not only did the radiance from a given detector have to exceed a signal-to-noise threshold, but so too did a sufficient number of surrounding values in order to produce moment statistics that were sufficiently pointlike. These criteria introduced a selection bias in the average flux measured for some of the stars by aggressively rejecting measurements near the S/N threshold on a given DCE. Noise will cause some of the measurements on a star with a true S/N close to the selection threshold value to be rejected. Consequently, the fluxes for the accepted values will average as too high. In an attempt to compensate for this bias, the DCE-averaged flux for any star that had fewer measurements than 0.9 times the total number of opportunities was rejected. Band E is most affected by this criterion, as may be inferred by comparing the NEIs listed in Table 2 with the fluxes in Table 3. For example, there were no valid mirror-scan band E observations of α Lyr, as all these were obtained well below the S/N ≥ 10 selection criterion. There were few band E observations of α CMa and β Gem within a given DCE; the small number of nonempty β Gem data sets were rejected, as were all but three of those for α CMa. Approximately a third of the α Tau and α Boo band E fluxes taken in the second half of the mission were also eliminated. In contrast, only a few DCE average fluxes in the other bands were rejected.

4.2. *CB06 Photometry*

Cohen et al. (2001) describe how stellar images were created from the CB06 DCEs for the individual scans. R. Walker (2002, private communication) provided us with the stellar images from the individual scans on a DCE, as well as the image obtained by co-adding all the scans on that star. Analogous to the mirror-scan processing, we extracted the flux from each scan image by fitting the point-response function. A mean and standard deviation about the mean were derived from the 19–20 fluxes thus extracted for each star on a given DCE.

Note that the photometry of Cohen et al. (2001) was obtained in an entirely different manner; they performed aperture photometry on the individual scan and co-added images. The S/N of the extracted photometry was used to

TABLE 3
GLOBAL *MSX* CALIBRATION OF THE CWW STELLAR STANDARDS

Star	Band A	Band B_1	Band B_2	Band C	Band D	Band E
α Boo.....	1.465×10^{-14} ±0.4%	5.598×10^{-15} ±0.7%	8.731×10^{-15} ±0.6%	1.719×10^{-15} ±0.3%	1.049×10^{-15} ±0.2%	6.635×10^{-16} ±0.8%
α Tau.....	1.281×10^{-14} ±0.4%	4.764×10^{-15} ±0.7%	7.417×10^{-15} ±0.6%	1.555×10^{-15} ±0.3%	9.474×10^{-16} ±0.2%	6.023×10^{-16} ±0.8%
α Lyr.....	8.109×10^{-16} ±0.5%	3.333×10^{-16} ±1.1%	5.339×10^{-16} ±0.9%	9.703×10^{-17} ±0.7%	5.901×10^{-17} ±0.6%	4.167×10^{-17} ±5%
β Gem.....	2.447×10^{-15} ±0.4%	9.550×10^{-16} ±0.8%	1.495×10^{-15} ±0.7%	2.830×10^{-16} ±0.5%	1.746×10^{-16} ±0.3%	1.195×10^{-16} ±2.7%
γ Dra.....	3.053×10^{-15} ±0.8%	1.123×10^{-15} ±1.1%	1.734×10^{-15} ±1.4%	3.703×10^{-16} ±0.7%	2.229×10^{-16} ±0.5%	1.462×10^{-16} ±2.2%
γ Cru.....	1.779×10^{-14} ±0.7%	6.310×10^{-15} ±0.9%	9.823×10^{-15} ±0.9%	2.221×10^{-15} ±0.5%	1.356×10^{-15} ±0.4%	8.610×10^{-16} ±1.2%
β And.....	5.271×10^{-15} ±1.6%	1.833×10^{-15} ±1.5%	2.997×10^{-15} ±1.8%	6.482×10^{-16} ±1.2%	3.964×10^{-16} ±1.2%	2.429×10^{-16} ±2.8%

NOTE.—Irradiance units are watts per square centimeter.

weight the individual images to create the co-added image and the range of fluxes from the individual scan images to express uncertainties. We, on the other hand, found that photometry obtained by a least-squares fit of the PRF to the star images from the individual scans produced smaller dispersions than the Cohen et al. aperture photometry. The CB06 PRF-fit photometry about the mission means had about half the scatter of the aperture photometry of Cohen et al. (2001).

4.3. *Correction for Trends in the Data*

The fluxes extracted for a star tended to be higher as the mirror scanned in one direction compared with the other within a DCE. Although present on many DCEs, the trend was not apparent in all bands for all DCEs, and the trend was not universally scan direction specific, that is, the flux is high in a specific direction and low in the opposite direction; the sense of which scan direction produced higher values changed from DCE to DCE and within a DCE. This behavior is likely due to the fact that the responses of the detectors in a column averaged to somewhat different values for each column. The standard deviation of the DCE mean could be reduced by taking the average of the fluxes from consecutive back-and-forth scans. Doing so reduced the number of independent measurements by a factor of 2, to a nominal 40 per DCE, but without significantly changing the DCE mean, and reduced the uncertainty in the mean by up to 10%.

The standard deviation of the individual measurements in a DCE about the mean is on the order 3%–5%. It was deduced that the DCE means had an additional measurement error from the fact that the standard deviation of the DCE means about the global mean did not scale according to Gaussian statistics from the individual DCE means. A close examination of the DCE-averaged stellar fluxes measured on the calibration experiments revealed an apparent variation in response during the mission. Since many of the components in equation (1) depend on focal-plane temperature, a residual variation after the temperature corrections in equation (1) would be consistent with what was observed.

Owing to spacecraft viewing constraints, no single CWW star had a sufficient number of measurements over the entire range in focal-plane temperature to produce a good solution to the response variation. Since the predicted fluxes of the CWW stars have their own set of uncertainties, scaling factors were derived and applied to the fluxes from α Boo, α Tau, α Lyr, and β Gem to normalize their *MSX* measurements to those of α CMa; β Peg was rejected as being variable, and γ Dra and γ Cru had too few observations to be useful. The α CMa fluxes were forced to be equal to the CWW values in Table 2. The stellar observations were normalized to α CMa by taking ratios of the stars and Sirius that were obtained on the same DCE and on different DCEs but at the same focal-plane temperature. The focal-plane temperature changes little during a DCE, so ratios from the same DCE should be free of temperature effects. Ratios of stars measured on different DCEs were also taken if they were in the same 0.5 K temperature interval, under the assumption that the SPIRIT III response was the same for all observations within this small focal-plane temperature interval. The scale factor between a given star and Sirius is the weighted average of the ratios determined by combining the results from both methods. Ratios obtained on the same DCE are doubly weighted, as these values are included directly in the averages and also within a given temperature bin. The averaging produces a single scale factor for each star in each spectral band and provides an initial evaluation of the photometric ratios in the CWW network. The ratios are applied to the stellar measurements to normalize the fluxes to that from Sirius, and a weighted least-squares polynomial is fitted through the result; the weights are the inverse variances of the individual DCE means. The multiplicative temperature correction to the response is then the in-band CWW flux for Sirius divided by the polynomial fit. This correction shifts the SPIRIT III calibration reference star from α Boo, a CWW secondary standard, to the primary standard, Sirius. Except for band E, the corrections to the measurement as a function of focal-plane temperature are small, at most 1%. The band E corrections range up to ±5%. An extreme example of the effect of correcting the response is shown in Figure 2, which plots a histogram of all the individual band E measurements of γ Cru before and after temperature correction.

5. THE GLOBAL MEAN FLUXES

The mission weighted averaged fluxes for seven infrared standard stars were calculated separately for the DC and CB observations and then combined into the global means listed in Table 3 (β Peg was not included, because it was measured to be variable). These fluxes are derived by requiring that the

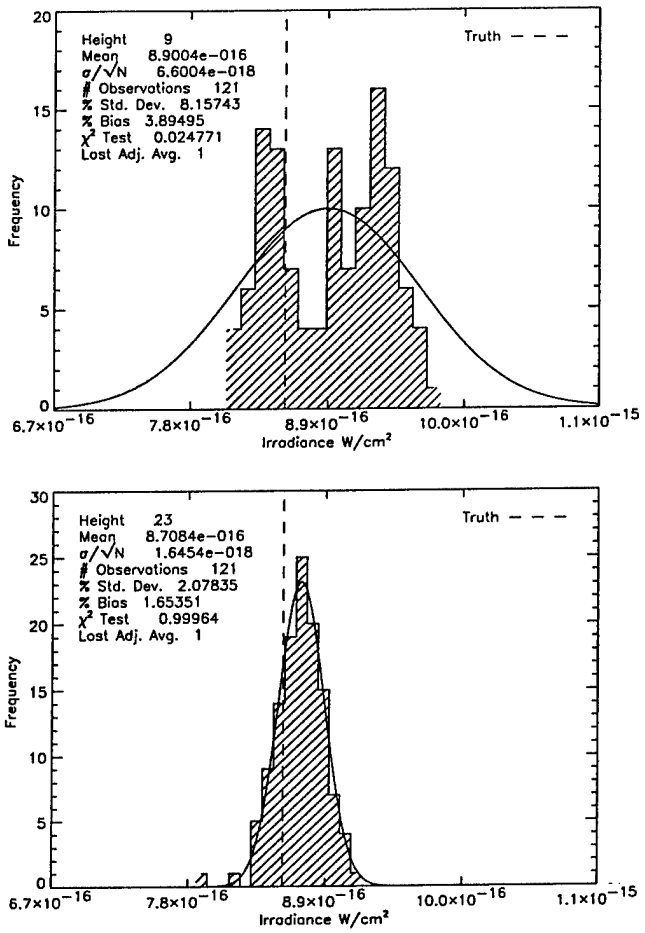

FIG. 2.—Histograms of the frequency of occurrence for the γ Cru band E fluxes before (*top*) and after (*bottom*) correcting for the temperature-dependent response. The histograms bin the 121 independent back-and-forth averaged fluxes obtained on three DCEs.

fluxes observed by *MSX* for α CMa be the same as those predicted for this star by CWW.

Separate tables of stellar magnitudes relative to α CMa with associated uncertainties were created from the DC and CB mission-averaged fluxes. For convenience, the common convention that the infrared magnitude of Sirius is -1.36 in all the *MSX* bands was adopted, which is equivalent to assuming that the flux from α CMa is 3.50 times that from the zero-magnitude standard star. The minimum of the average differences between stars in the two magnitude tables is the offset needed to scale the CB fluxes to the DC values. The CB06 values were scaled to the DC mirror-scan results in order to normalize the effective beam size of the point-response function in the CB06 PRF-fitted photometry. Specifically, the weighted average of the differences between corresponding entries for the same stars in the two tables is taken, where the weights are the root sum square of the standard deviations of the global means for the stars in the two tables. The CB06 values are scaled by the resulting offset, and a weighted average is taken of the two values for a given star. The averaged magnitude in a given band is then adjusted to force α CMa to have a magnitude of -1.36. Essentially, the logarithmic average is taken of the two data sets, and all the results adjusted relative to α CMa.

A reduced χ^2 analysis was used to check the consistency in estimating the errors. The sum of the squares of the differences between the scaled CB06 and DC magnitudes for each of the seven CWW stars was divided by the sum of the squares of the uncertainties associated with the two magnitudes. The square root of the result divided by the number of stars used for the calculation should be equal to 1 if the discrepancies are equal to the estimated error for each pair of stars. The average for all bands was 0.8; the individual values for each band indicate that the derived formal uncertainties in bands A, B_2, and E are a factor of about 2 too large, while those in bands B_1 and C are a bit too small. Thus, it may be concluded that the formal errors are accurate to within 50%.

5.1. *Measurement Precision*

The mission mean flux $\langle F \rangle$ of a star observed in M DCEs is calculated by

$$\langle F \rangle = \frac{\sum^M f_m w_m}{\sum^M w_m}, \quad w_m = \frac{N_m}{\sigma_m^2}, \tag{4}$$

where f_m is the mean flux from the mth DCE, which has a variance of σ_m^2 determined from N independent observations in the DCE. $N = 40$ for the large majority of DCEs.

The associated uncertainty $\varsigma_{\langle F \rangle}$ in the knowledge of the global mean flux measured for a star is

$$\varsigma_{\langle F \rangle} = \sqrt{\frac{\sum^M w_m (f_m - \langle F \rangle)^2}{M \sum^M w_m}}. \tag{5}$$

The uncertainty in knowledge of a DCE mean should be the standard deviation about the mean divided by a nominal $\sim$6.3 $(\sqrt{40})$ for the DCATT measurements and $\sim$4.4 $(\sqrt{20})$ for the CB DCEs. If the measurement process were entirely random, the distribution of the DCE means about the global mean would have a standard deviation given by equation (5), that is, equal to the average standard deviation of the individual means divided by the square root of the average number of independent measurements within a DCE. The fact that the formal solution using equation (5) produces standard deviations that are larger than this implies that the DCE means are subject to an additional unknown source of measurement error. Assuming that this error is random, we found that the uncertainty in the knowledge of the mission means derived from equation (5) could reasonably be modeled by adding a 1% uncertainty in quadrature with the DCE variances. Thus, the mission or global means were derived by replacing σ_m^2 in equations (4) and (5) with $\sigma_m^2 + (0.01 f_m)^2$.

We also included an additional term with the uncertainty in the global averages that expresses the sensitivity of the mean to the choice of the method used to process the data. Mean fluxes were derived using straight trimmed averages and weighted averages with and without the 1% contribution, plus means from histogram fits. The standard deviations in the global means derived using these different procedures are 0.2%, 0.8%, 0.6%, 0.3%, 0.1%, and 0.8% in bands A, B_1, B_2, C, D, and E, respectively. The final uncertainty ascribed to each global flux mean includes these values divided by $\sqrt{M}$ added in quadrature to the formal uncertainty in the knowledge of the weighted mean that includes the 1%.

TABLE 4
RATIO OF *MSX* MEASURED TO CWW PREDICTED FLUXES

Star	Band A	Band B_1	Band B_2	Band C	Band D	Band E
α CMa	1[a]	1	1	1	1	1
α Boo	1.0015	1.0057	0.9907	0.9908	0.9908	0.9838
α Tau	0.9795	1.0294	1.0060	0.9903	0.9942	0.9962
α Lyr	0.9893	1.0164	0.9954	1.0479	1.0378	1.172
β Gem	0.9800	0.9786	0.9487	0.9907	0.9909	1.088
γ Cru	0.9738	1.012	1.001	0.9987	0.9976	1.005
γ Dra	0.9812	1.0398	1.0069	0.9931	0.9772	1.0245
Average	0.986	1.014	0.990	0.991	0.988	1.023
$\sigma/\sqrt{N}$	±0.008/2.24	±0.021/2.24	±0.021/2.24	±0.001/2.0	±0.007/2.0	±0.04/2.0
	±0.004	±0.009	±0.010	±0.0005	±0.003	±0.020

[a] By definition.

5.2. *Results for the CWW Primary and Secondary Standards*

Table 4 lists the ratios of the measured global mean fluxes for the stars listed in Table 3 and the CWW predictions in Table 2. The averages over the stars in the table exclude the values for α CMa, to which the fluxes were normalized, the γ Cru ratios, and the band C, D, and E fluxes for α Lyr. M. Cohen (2004, private communication) renormalized the Cohen et al. (1996) γ Cru spectrum using *MSX* photometry from the CB06 analysis in Cohen et al. (2001). Since the CWW γ Cru fluxes we use in the present analysis are not independent of the *MSX* measurement that we are evaluating, we removed γ Cru from the averages in the table. We include the best-fitting of the two γ Cru spectra that Cohen provided for qualitative comparison. The correction to the response as a function of focal-plane temperature was not applied to the γ Cru photometry in Cohen et al. (2001), which could have affected the overall scaling that may be the difference between these two most recent spectra. Also, the dispersion in the measurements is much greater without the responsivity correction, as may be seen in Figure 2. However, γ Cru is the brightest of the calibration stars, so we include it in the qualitative comparisons. The star β Peg was also removed because of its apparent variability (see § 5.2.2).

The uncertainties in the averaged ratios are expressed in two ways in the last two rows of the table. The first line displays the rms of the fluxes about the average, which is followed by a slash and the square root of the number of fluxes in the average. The second entry does the division to derive the uncertainty in the average.

The biases obtained by subtracting 1.0 from the flux ratios in Table 4 are plotted for each star in Figure 3. The solid error bars are the values derived from the uncertainties for each star listed in Table 3; the dotted error bars are those assigned by CWW for the *MSX* in-band uncertainty from the absolute CWW spectra for the stars. The dashed line is the bias in the *MSX* measured offset for the star from the CWW predictions. The bias was determined from the average of the measured band C and D fluxes because they should be measures of the continuum for these stars and have the smallest uncertainties in Tables 3 and 4. Since the biases are generally within the errors that CWW assign to their absolute spectra, it may be said that the *MSX* observations validate the CWW calibration spectra relative to α CMa.

As may be seen from Table 4, the average of the measured divided by the predicted fluxes for the *MSX* CWW calibration stars is ~1% low, a ~3 σ result. The band A ratio for α Lyr is also about 1% low. Since the infrared flux of α CMa in Cohen et al. (1992a) is derived from α Lyr, the average ratio for all the stars and that for α Lyr in band A can all be brought into agreement by simply increasing the flux for Sirius by 1%. This is within the 1.46% bias error that Cohen et al. (1992a) assign to the absolute scale of the Sirius spectrum.

The *MSX* [X]−[D] magnitude differences for the CWW stars measured by *MSX* are plotted as a function of spectral type in Figure 4. K0 is designated as 0 on the spectral type scale, K5 as 5, M0 as 6, and the latest spectral type, M3.4, as 9.4. Band D was chosen for the fiducial because, next to band A, it has the highest-quality measurements on these stars and is in a continuum region. The *MSX* measurements are plotted as plus signs with the associated error bars, and the CWW values are plotted as diamonds. The dashed line is a least-squares linear fit through the *MSX* values, while the dotted line is the magnitude difference predicted by the Engelke function (Engelke 1992) using the effective temperatures given in Table 1. The Engelke function is an analytic representation for the infrared continuum for stars in which H^- opacity dominates. The systematic variation of the measured [A]−[D] and [B_1 or B_2]−[D] from the continuum Engelke function with spectral type primarily reflects the influence of molecular absorptions in the stellar atmosphere. Band A contains the SiO fundamental absorption band and the 6.3 μm water vapor band, which are present in all the stars with composite spectra. The difference in bias between bands B_1 and B_2 in Table 4 averages to 2.25% with an rms uncertainty in the mean of 0.8%. Band B_2 has a larger spectral bandpass and covers more of the CO absorption band in cool stars, which may qualitatively explain the difference. Cohen has assigned large uncertainties, on the order of 10%, to these bands because the atmosphere is opaque at these wavelengths and accurate spectral observations are lacking. The stellar CO absorption profile is steepest across these bands and the integrated flux is very sensitive to any spectral shifts. The continuum colors, [C]−[D] and [E]−[D], agree with the predictions of the Engelke function to within the measurement errors, and the *MSX* and CWW values correlate well, even for the B bands, considering the large errors Cohen et al. assign to the composite spectra at these wavelengths.

5.2.1. *Flux Excess*

The measured fluxes for α Lyr in bands C and D deviate at the 6–7 σ level from the continuum predictions in Cohen et al. (1992a). The band C excess may be due to a small residual flux bias overestimate, as the mirror-scan observations in this band

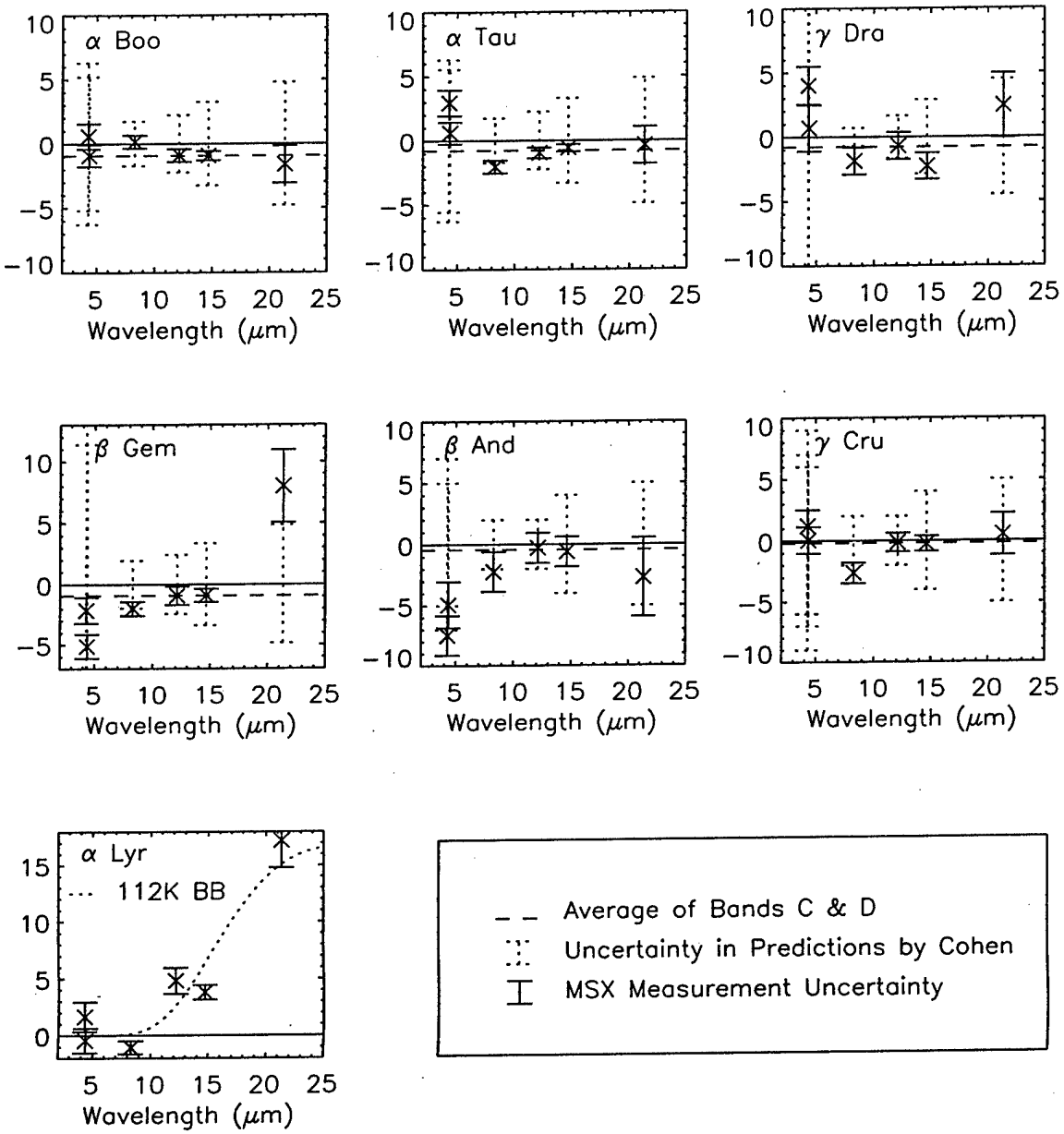

FIG. 3.—Percentage biases in the *MSX* fluxes measured for the standard stars from Table 4. The measurement error bars are the solid lines, and the dotted error bars are the CWW values. The solid horizontal line defines where the measurements would equal the predictions; the dashed line is the bias of the *MSX* measured offset for the star from the CWW predictions.

failed the 0.90 times the number of measurement opportunities test for focal-plane temperatures above 11.6 K. However, band D measurements had no such problems. The only valid band E measurements were from the CB06 observations. Plausibly, excess emission from Vega's debris ring may contribute to the continuum flux at these shorter wavelengths. Heinrichsen et al. (1998) combined ISOPHOT 25–200 μm photometry on Vega with *IRAS* and submillimeter observations to model the flux excess from the dust ring as a 73 K blackbody modified by a $\lambda^{-1.1}$ emissivity, which fit their measured 25 μm flux excess of ~50% above the Kurucz model continuum adopted by CWW for Vega. The 17% band E excess in Table 4 is entirely consistent with this model. The Heinrichsen et al. model predicts a band D flux excess from the dust ring of only ~1.5%, compared with the observed excess of 4%. However, the 4% excess in this band is consistent with the 100 K blackbody fit through the data in Figure 2 of Heinrichsen et al. (1998).

The 1.6% discrepancy between the band B_1 fluxes for α Lyr and α CMa in Table 4 is marginally statistically significant at the 2 σ level. The cause of this discrepancy is unclear but may be related to sensitivity, as the CWW model spectra for α Lyr and α CMa in the more sensitive band B_2 are entirely consistent with the *MSX* measurements.

5.2.2. *Variability*

Variability is a critical issue, as the brightness of standard calibration stars is usually taken to be constant. Of the CWW stars measured by *MSX*, only β Peg was found to change its flux during the mission, as may be seen in Figure 5, in which the β Peg DCE mean fluxes are plotted as a function of time.

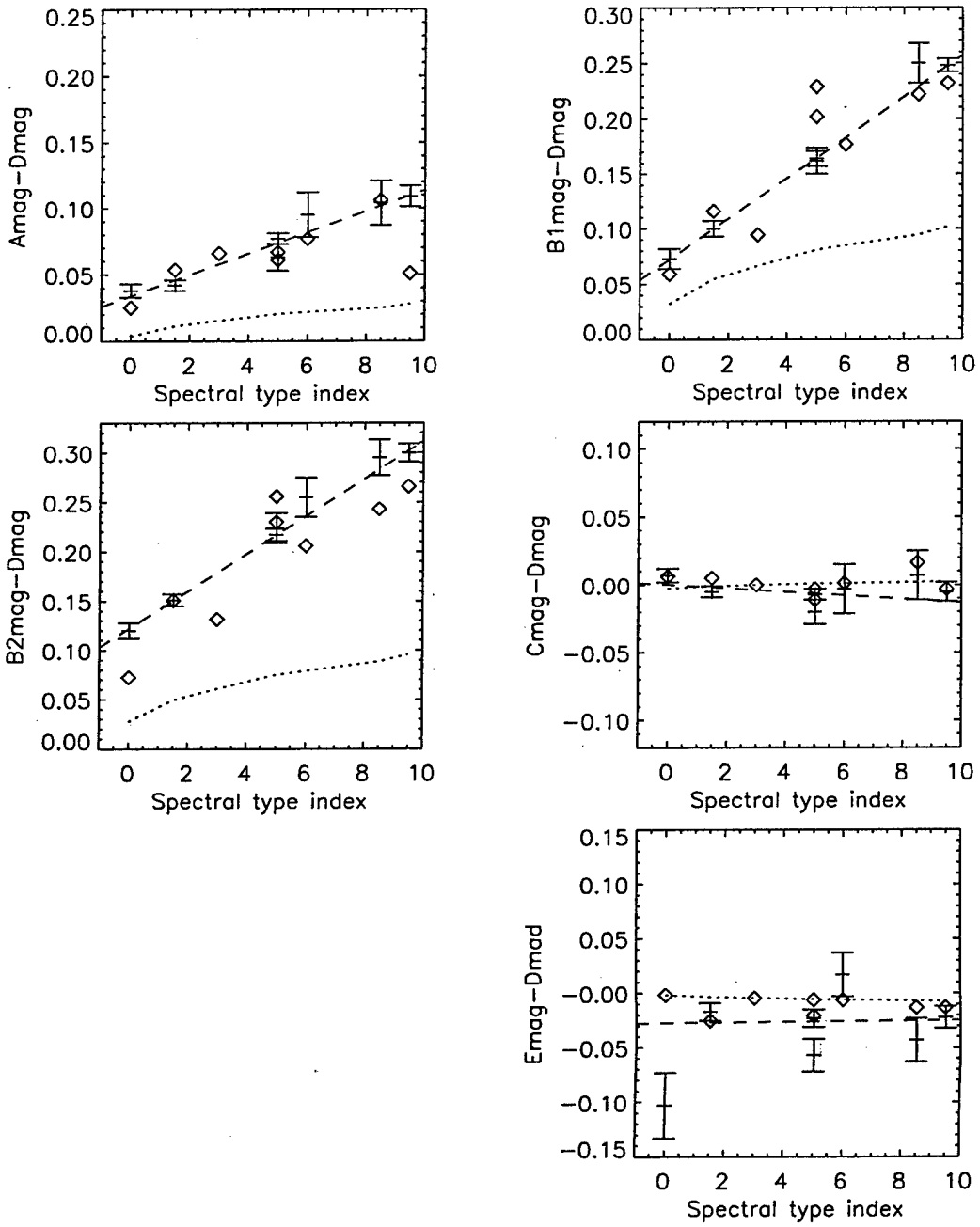

FIG. 4.—Correlation between *MSX* magnitude differences with respect to band D and spectral type. Diamonds are CWW values; plus signs with error bars are *MSX* measurements. The dotted lines are the Engelke function, and the dashed lines are least-squares fits through the measurements.

A clear time-dependent correlated variation of ~8% is evident across all *MSX* bands.

This star is listed as an optical variable in the SIMBAD database but has not been previously reported in the literature to vary significantly in the infrared. Smith (2003) extracted *COBE* DIRBE near- to mid-infrared photometry of the brightest 12 μm sources out of the Galactic plane, including that for β Peg. The DIRBE β Peg flux indicates a 3% variation, at most, during the 10 month *COBE* mission, a period comparable to the cryogenic lifetime of SPIRIT III. Smith (2003) determined that the formal solution for the amplitude of variability for this star was 2%–4%, which was within the 1 σ (mid-infrared) to 2 σ (near-infrared) in the solution. Since no similar variation was observed for the other CWW standard stars measured during the *MSX* calibration experiments and the uncertainties in global means for the well-observed stars in Table 3 are very small, we deduce that either the amplitude of the variation of β Peg changed between the epochs of the *MSX* and *COBE* observations or the *COBE* observations are centered on one of the extrema in the infrared light curve. M. Cohen (2004, private communication) notes that archival *N*-band photometry from the Air Force Maui Optical and Supercomputing Site between 1980 and 1993 indicated an episodic 0.1 mag brightening for this star.

Smith (2003) found no statistically significant variations in the DIRBE photometry for γ Cru, or any of the other stars in

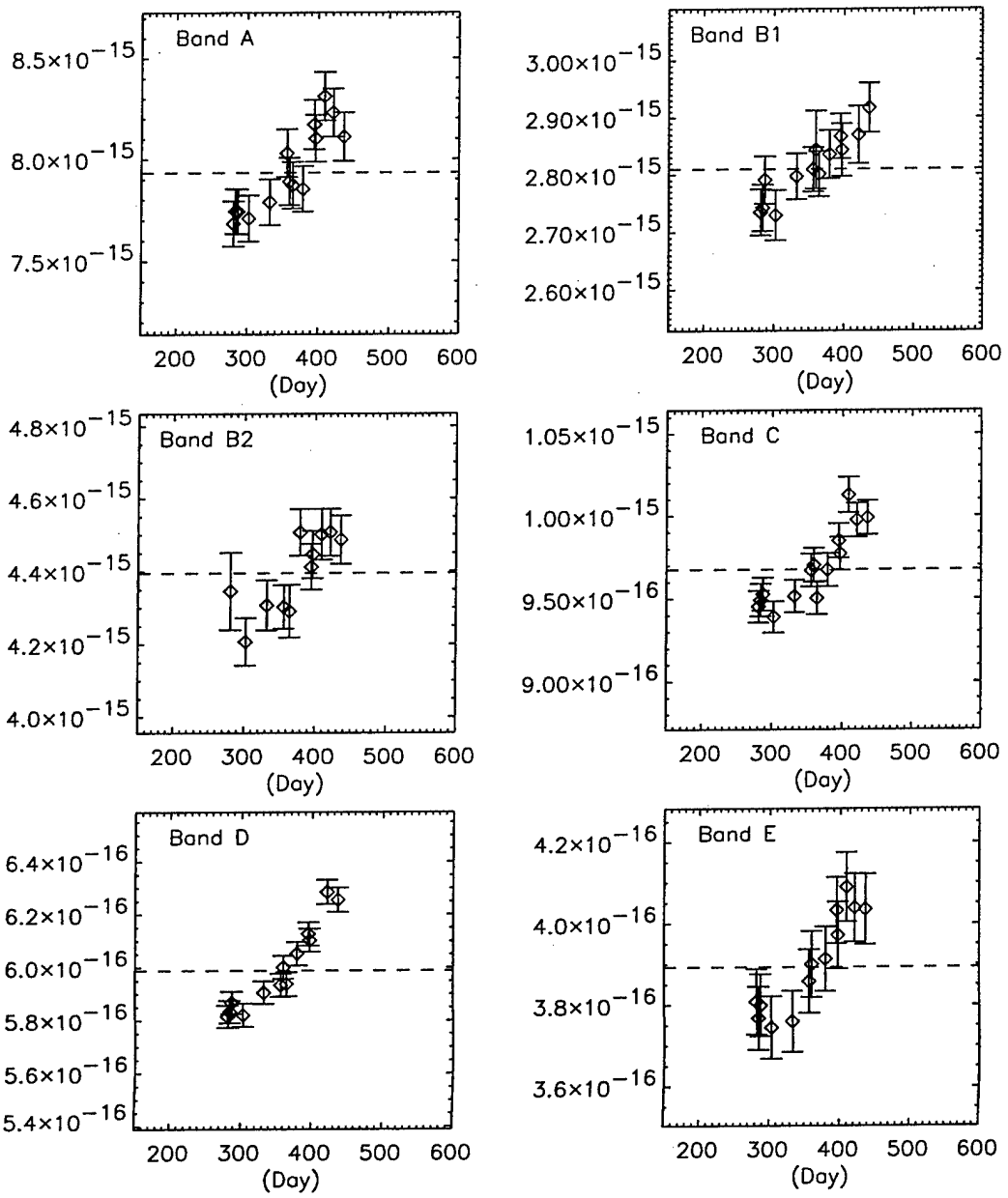

FIG. 5.—Time variation of the β Peg DCE means. The dashed line is the mean of the data points.

Table 2, during the *COBE* mission in the DIRBE data set. This finding is especially important for γ Cru, which is of a later spectral type than β Peg and would be expected to show more variability.

5.2.3. *Stars with Spectral Templates*

A principal objective of the CB06 experiment was to validate the use of template spectra for stars based on composite spectra of standard stars of the same spectral class. Cohen et al. (2001) measured 33 fainter stars in the calibration network (Cohen et al. 1999) in the CB06 experiment that had calibrated template spectra. This was a reasonable sample of 7.5% of the stars in the 1999 network. The differences between the *MSX* measured in-based fluxes and those based on the template spectra ranged between 0% and 8% with an rms of 3% and an average bias of 2%. We repeated this analysis using PRF-fitted photometry after correcting the images for temperature-dependent response on the 23 stars for which we could obtain reliable results from the individual scans. The measurements had essentially the same scatter (2.8%) but with a smaller range of deviations. However, our measured values agreed on the average with the predicted values (ratio = 0.999).

6. REFERENCE SPHERES

The infrared flux from an emissive reference sphere is determined by the physical properties of the sphere, the range with respect to the *MSX* spacecraft, and the thermal balance between incident radiant energy absorbed by the sphere and that radiated away. The governing equation for the thermal

balance that expresses the temperature of the sphere, T, as a function of time, t, is

$$V\rho C_p(T)\frac{dT}{dt} = \text{Area}[(1-A)F_{\text{Sun}}(\tfrac{1}{4} + af_{\text{Earth}}) + \epsilon_{\text{sphere}}\epsilon_{\text{Earth}}F_{\text{Earth}} - \epsilon_{\text{sphere}}\sigma T^4], \quad (6)$$

where V and Area are the volume and area of the sphere, respectively; ρ is the density of aluminum (2.7 g cm^{-3}); C_p is the specific heat of the sphere, which is calculated from Debye theory; A is the Bond albedo of the sphere; F_{Sun} is the amount of solar flux incident on the sphere; af_{Earth} is the solar flux reflected from the sunlit Earth with a Earth's geometric albedo and f_{Earth} a geometric factor that expresses the fraction of Earth seen by the sphere that is illuminated by the Sun; ϵ_{sphere} is the mean infrared emissivity of the sphere; $\epsilon_{\text{Earth}}F_{\text{Earth}}$ is the upwelling Earth radiation incident on the sphere; and σ is the Boltzmann constant.

Equation (6) may be rewritten in terms of the equilibrium temperature, T_{eq}, that would be the instantaneous temperature of the sphere if it had no thermal mass:

$$\frac{V\rho C_p(T)}{\sigma \times \text{Area} \times \epsilon_{\text{sphere}}}\frac{dT}{dt} = \frac{1-A}{\sigma\epsilon_{\text{sphere}}}F_{\text{Sun}}\left(\frac{1}{4} + af_{\text{Earth}}\right) + \frac{\epsilon_{\text{Earth}}F_{\text{Earth}}}{\sigma} - T^4 = T_{\text{eq}}^4 - T^4. \quad (7)$$

This nonlinear differential equation has the boundary condition that the sphere temperature at the time of ejection has to equal the measured value. The initial temperature ranges from 259.5 K for ERS1 to 258.3 K for ERS5. A Runge-Kutta integration was used to solve the differential equation in 50 s time steps. The 50 s time interval is quite adequate, as it is much smaller than the characteristic thermal time constant in the thermal balance equation:

$$\tau = \frac{V\rho C_p(\bar{T})}{4\sigma \times \text{Area} \times \epsilon_{\text{sphere}}T_{\text{eq}}^3} \sim 1800 \text{ s} \quad (8)$$

(Kintner & Sohn 1993b). There are approximately eight observations within the 50 s time increment. The result at the time of an observation is interpolated between bracketing solutions to the equation.

Kintner & Sohn (1993a) solved equation (6) using nominal or idealized parameters to explore the characteristics of the solution, especially the sensitivity to uncertainties in the input parameters. Chalupa et al. (1991b) described a similar gray-body thermal analysis of a sphere deployed from another satellite. This experiment was not flown, but the present analysis is based, in part, on the model formalism developed by these authors. Kintner & Sohn (1993b), Chalupa et al. (1991a), and Chalupa & Hamilton (1993) provide a more complete and detailed exploration of the model.[5]

6.1. *Physical Characteristics of the Emissive Reference Spheres*

The reference spheres were made of 6061-T6 aluminum. The manufacturing specification was for the spheres to be 1 cm in radius with a tolerance of ±0.01 cm. The density of the spheres was assumed to be that of aluminum, 2.7 g cm^{-3}. The temperature-dependent specific heat was calculated using Debye theory (see, e.g., Kittel 1986, pp. 131–141), in which $C_p = \gamma\sqrt{T} + A(T)T^3$, where γ and $A(T)$ were chosen to reproduce the thermal capacities of aluminum at the various temperatures listed in the Handbook of Chemistry and Physics (Hodgman et al. 1957). Marquardt et al. (2001) fitted the various published values of the specific heat of 6061-T6 aluminum between 4 and 300 K with an eighth-order polynomial in the logarithm of the temperature, with a cited error in the fit of 5%.[6] Over the 260–285 K range of interest, the NIST values are ~4.4% higher than the Debye calculations. We split the difference and scaled the Debye values by 1.02, adopting an uncertainty of 2.2%.

The emissive reference spheres are coated with Martin Black. Wilson (1992) describes the ground-based measurements that characterized the thermal and emissive properties of the reference spheres. Directional spectral reflectivity measurements on witness samples coated with Martin Black were performed by the Surface Optics Corporation (SOC), the results of which are in an SOC (1993) technical report. Also, direct measurements of the effective emissivity for the witness sample over all angles and wavelengths were carried out at the Low Background Infrared (LBIR) Facility of the National Institute of Standards and Technology (NIST 1993). The witness samples were fabricated of the same aluminum as the spheres and coated with Martin Black at the same time as the spheres. These spectral reflectivity measurements are in substantial agreement with the published measurements of Pompea et al. (1984) taken at lower spectral resolution. Martin Black has a very low reflectivity throughout the visible, less than 1%, with comparable values in the mid-infrared between 6 and 40 μm. However, the reflectivity is significantly larger between 1 and 6 μm and at wavelengths longer than 50 μm. The SOC measurements and the bidirectional reflectance measurements of Bartell et al. (1982) at 10.6 μm show that the infrared reflectivity is also a strong function of scattering angle, increasing roughly as the secant squared as the scattering angle is increased from 0° to 80°.

Kintner & Sohn (1993a) describe the calculation used to determine the mean infrared emissivity of the sphere and the absorption efficiency to solar flux. The wavelength- and angle-dependent reflectivity of Martin Black was weighted by the solar spectrum and integrated over wavelength and a hemisphere to derive the Bond albedo and absorption efficiency (1 − Bond albedo) for the sphere. E. Kintner (1993, private communication) derived a Bond albedo of $A = 0.069$ based on the SOC measurements, and we adopt the consequent value of 0.931 for the absorption efficiency of the sphere to solar flux. A similar calculation using a 300 K blackbody for the spectral weighting function was performed to derive an effective infrared emissivity of 0.97. A blackbody of this temperature was assumed to be representative of the mean thermal emission from Earth. The total hemispherical infrared reflectivity of a Martin Black–coated witness sample was measured to be 0.046 in the NIST LBIR Facility.[7] The NIST-measured effective infrared emissivity is, therefore, 0.954. We adopt a mean emissivity that is the average of the two values, $\epsilon_{\text{sphere}} = 0.962$ with an uncertainty of 1%.

[5] These three company technical reports were given limited distribution and likely are not available. However, these reports contain analytic expressions applicable to the problem that were derived by the authors. Reference is given to the documents to properly credit the authors for their insight.

[6] See http://cryogenics.nist.gov/NewFiles/6061_T6_Aluminum.html.

[7] The measurement geometry is shown in Fig. 7 of http://physics.nist.gov/TechAct.Archive/TechAct.93/844h.html.

Using an average infrared emissivity in the energy balance equation is reasonable, as it accounts for the spectral properties of the sphere outside the 6.8–25.1 μm wavelength range spanned by the *MSX* bands. However, the wavelength dependence must be included in determining the irradiances in the *MSX* spectral bands. The emissivity of Martin Black over *MSX*'s mid-infrared wavelengths was determined from the SOC measurements to decrease roughly linearly from about 0.981 at 6.7 μm to 0.954 at 16 μm and to remain at this value out to 26 μm. The phase function needed to calculate the amount of sunlight and earthshine reflected by the sphere to SPIRIT III was assumed to be equal to the illuminated fraction of the sphere as seen by the sensor.

Since the solar source function gives low weights to the contributions from wavelengths greater than 30 μm, which are poorly determined for Martin Black, we estimate that the uncertainty in the absorptivity is less than 1%. As noted above, the uncertainty in the infrared emissivity of the sphere is also estimated to be 1%. The pertinent quantity in the time-dependent solution is the coefficient of the differential on the left-hand side of equation (7); that is, the thermal mass ($V\rho C_p$) divided by Area $\times \sigma\varepsilon_{\text{sphere}}$. The uncertainty in V/Area is the 1% uncertainty in radius. The root sum square of this value with the 1% uncertainty in the infrared emissivity and the 2.2% in the heat capacity is about 2.7%.

6.2. *Thermal Input from the Sun*

A solar constant of 1367.28 W m^{-2} is adopted based on the mean values derived by Schatten & Orosz (1990) and Tobiska (2002), for which they show a mean variation of less than 0.1%. The solar constant is scaled by the inverse square of the heliocentric distance, in AU, at the time of the experiment. The factor of $\frac{1}{4}$ in equations (6) and (7) arises because the amount of solar radiation intercepted by the sphere is equal to its cross-sectional area whereas the equations are normalized to the surface area.

We assume that 80% of the sunlight reflected from Earth is diffuse and 20% is specular. The portion of Earth visible to the sphere is divided into approximately 51,000 surface elements, and the contributions from all the elements are summed to derive the diffuse component. That is,

$$af^{D}_{\text{Earth}} = 0.8a \sum_{da} \frac{\cos\alpha \cos\beta}{d^2} da, \qquad (9)$$

where a is the average amount of solar flux reflected by Earth, that is, Earth's geometric albedo, d is the distance from the sphere to the surface area element, da, on Earth, and α and β are the angles between the local vertical of the surface area element and the direction to the Sun and sphere, respectively. The summation is restricted to surface elements for which $\alpha \leq 90°$.

We adopted the analytic expression derived by Chalupa et al. (1991a) for the specular reflected component, which is based on the dispersion of incident parallel rays from the Sun by a spherical Earth of radius R_E. The result is

$$af^{S}_{\text{Earth}} = 0.2a \frac{R_E^2 \cos\alpha}{(2d + R_E \cos\alpha)(2d\cos\alpha + R_E)}. \qquad (10)$$

Again, α is $\leq 90°$.

The uncertainty in the direct solar flux absorbed by the sphere is essentially the uncertainty in the absorption efficiency, which is ~1%. The estimated uncertainty in the reflected component from Earth is dominated by the imprecise knowledge of Earth's geometric albedo. Initially, we used a mean value of $a = 0.4$, essentially the same as the de Pater & Lissauer (2001) value of 0.37. However, the various Earth resource satellite measurements available on the Web indicate that the local values on Earth can deviate by a factor of 2 from the mean. Specifically, the albedo is 0.2–0.25 in the tropics and increases with latitude, reaching a value of 0.8–0.85 at the poles. We approximated this latitude-dependent variation for the geometric albedo by the simple analytic expression $0.2 + 0.65\sin^6(\text{latitude})$. Fortunately for the error analysis, *MSX* and the spheres are in a dawn-dusk orbit and much less than the half of Earth visible to the sphere is sunlit during the experiments. Sunlight reflected by Earth constitutes 1% or less of the thermal input to the sphere for ERS3 through ERS5. It is on the order of 10% at the beginning of the ERS1 and ERS2 experiments, but the contribution becomes insignificant or nonexistent by the middle of these experiments. Thus, sizable 20%–30% uncertainties in evaluating this component result in small changes in the total thermal input to the sphere.

6.3. *Upwelling Radiation from Earth*

The upwelling Earth radiation is derived from the narrowband infrared measurements obtained by the Advanced Very High Resolution Radiometer (AVHRR) on the polar-orbiting NOAA *POES* satellite. NOAA creates thermal maps of Earth every 3 hours, and the maps closest to the start time of each of the ERS DCEs were used. Thus, the maximum time difference between a thermal map and a measurement within a DCE was 2 hours.

The thermal radiation from Earth is calculated at the time the spheres were ejected and at 50 s intervals thereafter; a total of 50 such calculations span the duration of the entire DCE. At each of these times the latitude, longitude, and altitude of the sphere are derived from the orbit calculated for the sphere. These parameters are used to determine the circular sector of Earth underneath the sphere. A coordinate system with the nadir of the sphere as the pole is adopted, and the AVHRR 11.5 μm map is centered on the nadir latitude and longitude and projected into those coordinates. A 300×325 grid is overlaid on the Earth visible from the sphere, the AVHRR data are binned onto this grid, and "over the horizon" values are eliminated. Analogous to equation (9), the 11.5 μm AVHRR radiance within each grid element is weighted by the cosine of the angle between the vertical of the area element and the direction of the sphere times the area of the element divided by the square of its distance. This quantity is then summed to derive the total 11.5 μm flux onto the sphere.

The integrated flux is converted into a brightness temperature by inverting the blackbody equation. The source function for the hard Earth is assumed to have a blackbody spectral energy distribution with a temperature equal to 1.05 times the 11.5 μm brightness temperature thus derived. The MODTRAN code (Berk et al. 1989) is used to calculate the transmission of the atmosphere to this source function, producing a representative spectral energy distribution from Earth at a single time index. Increasing the 11.5 μm brightness temperature by 1.05 compensates for the ~80% transmission that MODTRAN predicts for upwelling radiation from Earth at this wavelength.

The AVHRR 11.5 μm map used for ERS1 analysis is shown in Figure 6 along with the ground track for the sphere. Cool areas are bright and the darker areas are at warmer temperatures.

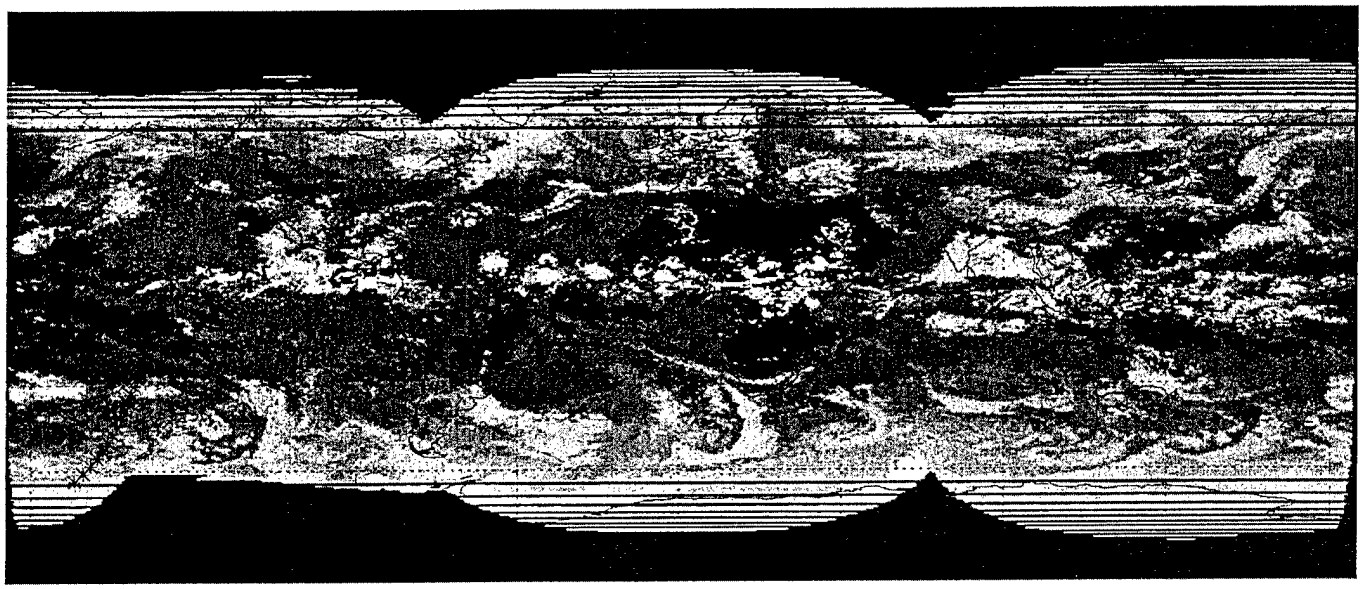

FIG. 6.—AVHRR 11.5 μm map used to calculate the upwelling Earth thermal radiation intercepted by ERS1. This is the day 238, hour 15 map, for 1996 August 25; the ERS DCE was executed between 1334 and 1413 UT that day. The ground track of the sphere is also shown.

The black strips at the poles are missing data, values for which are interpolated from surrounding values. The evolution of the spectrum of upwelling radiation during the DCE is shown in Figure 7. A spectrum is calculated at 50 s intervals from the time the sphere is ejected, and the spectral flux is interpolated between time indices in this plot. The derived spectrum is strongly influenced by absorptions from atmospheric ozone, by CO_2 at 4.3 and 15 μm, and by water vapor. As may be seen, the thermal flux from the cold polar regions is about half that from the tropics. The subtle variations in the overall flux level in the plot show the influence of cool clouds in the AVHRR data.

The thermal input to the sphere from Earth, as well as that from the sunlight reflected by Earth, is interpolated between two successive time indices to the time *MSX* observed the sphere. The direct thermal input from the Sun is constant.

6.4. *Measurement Geometry and Orbit of the Sphere*

A spring-loaded ejection mechanism deployed the spheres at a nominal velocity of 14.2 m s^{-1} in the *MSX* orbital plane at an angle of 15° above the spacecraft velocity vector. The sphere was retained by a three-point capture system. A thermistor in one of the contacts of the capture system measured the temperature of the sphere up to the moment of release. Photodetectors with beams placed in tandem at the end of the ejection tube measured the ejection velocity to an estimated accuracy of ±1%. The spheres were kept in an optically clean environment under dry nitrogen from the time they were fabricated until *MSX* was flown. The optically hygienic environment was maintained on the spacecraft until each sphere was ejected.

Velocities between 14.03 and 14.86 m s^{-1} were measured on the ground acceptance testing for the six ejector mechanisms flown on *MSX*. The measured ejection velocities had an average of 14.525 m s^{-1} with a 0.34 m s^{-1} standard deviation. Ejection velocities were measured on-orbit for four of the five spheres. (A reflective gold-coated sixth reference sphere failed to deploy during the mission, and the photodetector system for ERS4 failed.) The on-orbit velocities for the four spheres were

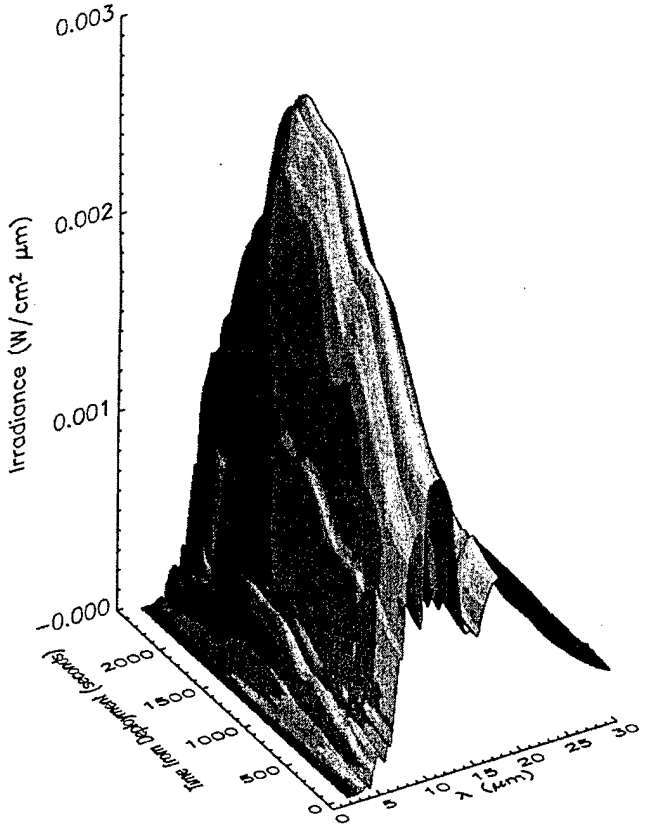

FIG. 7.—Time evolution of the spectral infrared flux from Earth incident on ERS1. Wavelength is along the x-axis, time along the y-axis, and flux along the z-axis. The variations in the fluxes are due to the poles having a lower temperature than the equator, that is, the flux being higher in the middle, and cloud cover.

consistently ~0.4 m s^{-1} smaller (to within ~0.06 m s^{-1}) than their acceptance test values. The implication is that whatever caused the change in the velocities between the acceptance tests and the on-orbit experiments, it was essentially the same for all the spheres. It may have been that the energy stored in the springs decreased by a small amount (~1.5%) as a result of environmental changes between the ground test and in-flight. The ejector mechanisms were ~35 K colder on the spacecraft than on the ground and operated in a vacuum. We infer that while knowledge of the ejection velocity may be biased a percent or so, the relative velocities of the spheres are known to better than 1%.

According to Abbot et al. (1997), the *MSX* spacecraft was generally tracked by radar to a positional accuracy of better than ~15 m during the reference-sphere DCEs. Thus, any relative range errors to the spheres were dominated by the uncertainties in the sphere ejection velocity and, to a much lesser degree, deployment angles. *MSX* was programmed to center the sphere on the SPIRIT III mirror-scan field of regard assuming that the sphere was ejected at 14.5 m s^{-1} at azimuth and elevation angles of 0° and 15°, respectively. The Space-Based Visible (SBV) sensor[8] on *MSX* was only able to briefly track ERS3; SBV did not track the other spheres, because they were too faint. This limited observation could only indicate that ERS3 was within 5% of its nominal trajectory. Only ERS4 was measured to have an anomalous azimuthal deployment angle, of about ~2°, as determined from the in-scan position of the spheres in the field of regard as a function of time. Mavrofrides et al. (1998) noted that such a small azimuthal error has virtually no effect on the range to the sphere. However, they did find that an error in the assumed 15° vertical deployment angle produces a relative flux error that is roughly proportional to 0.2 times the relative angle error; for example, a 2° elevation error they examined translated into ~3% flux error. The relative flux error is twice as large as the relative error in the ejection velocity. Unfortunately, the elevation and azimuth angle measurements of SPIRIT III and SBV poorly constrain the uncertainties in the ejection velocity and deployment angles.

6.5. *Estimated Uncertainties in the Model Predictions*

The accuracy in the model predictions of the irradiances in each *MSX* band is a sensitive function of the error in determining the temperature of the sphere. It is also proportional to the uncertainty in the infrared emissivity and the square of the error in the radius of the sphere, and inversely proportional to the square of the range error. Kintner & Sohn (1993a, 1993b) and, independently, Chalupa et al. (1991a) and Chalupa & Hamilton (1993) performed sensitivity analyses on each of the thermal and geometric components of the model. They used analytic expressions for the various thermal inputs and adopted values with rather generous uncertainties for each of the parameters in equations (6) and (7) to demonstrate that the modeled fluxes could be predicted to within the program goal of 10% for in-band absolute flux accuracy, 3% accuracy in the band-to-band ratio, and 3% in precision. The differences between the model parameter values we use and those adopted in these sensitivity analyses deviate by usually no more than the uncertainties used in the sensitivity analyses. Thus, the absolute accuracy of the model has been shown to be at least as good as 10%.

[8] See http://www.ll.mit.edu/ST/sbv/sbv_table_of_contents.html.

However, the accuracy is demonstrably better than this. The largest sources of error in these analyses were the uncertainties in the amount of sunlight reflected by Earth and the thermal flux from Earth. The thermal radiation from Earth in our model is known to a much higher accuracy than the ~10% adopted in the sensitivity analyses. Also, the uncertainty in the most poorly known component, that of the reflected sunlight, is mitigated by the fact that this component contributes very little to the thermal input to the sphere. We estimate that the uncertainty in the calculated temperature of the sphere is about 1 K, which is commensurate with the uncertainty in the initial temperature and is about half the ~2 K uncertainty obtained by Kintner & Sohn (1993a, 1993b). A temperature error of 1 K results in a 2.3% error in band A, with progressively smaller errors with wavelength band to ~1% in band E.

The estimated uncertainties in the modeled fluxes are 4% in band A, 3.5% in bands C and D, and 3% in band E, about 3 times smaller than those derived in the sensitivity analyses of Kintner & Sohn (1993a, 1993b) and Chalupa & Hamilton (1993). These values are the root sum square of the flux uncertainties arising from the precision in the fluxes from the 2% in the cross-sectional area of the sphere, another 2% in the square of the range, the estimated uncertainty in the wavelength-dependent emissivity, and the flux uncertainty from a 1 K error in the knowledge of the temperature of the sphere. A 1 K temperature uncertainty at a nominal 270 K sphere temperature translates into flux uncertainties of 2.3%, 1.7%, 1.4%, and 1.1% in bands A, C, D, and E, respectively. The wavelength-dependent emissivity is known with an accuracy of about 1.5% in band A and improves with wavelength to ~1% in band E.

6.6. *Calibration against the Emissive Reference Spheres*

The in-band radiance predicted by the model at the time of each observation is obtained by integrating over wavelength the product of the wavelength-dependent emissivity, the normalized spectral response of the bands, and the spectral energy distribution from the blackbody at the temperature of the sphere predicted by the thermal balance equations. This is converted to flux by multiplying by the solid angle subtended by the sphere at the distance derived from the sphere's trajectory. To this is added components from the direct sunlight, the sunlight reflected by Earth, and the upwelling Earth radiation, all of which are reflected by the sphere at the time of observation. The reflected component from the upwelling Earth radiation is much more than 10 times that from the Sun over the *MSX* mid-infrared bands, but the sum of the two constitutes 1% or less of the total predicted in-band flux. The calculated spectral fluxes from Earth, such as those in Figure 7 for example, are used in the calculation.

The ERS1 measurements in each of the four *MSX* mid-infrared spectral bands are shown in Figure 8. The data points are plotted with their associated error bars; estimated uncertainty bounds to the model predictions are plotted as the solid lines. As with the stellar observations, successive back-and-forth measurements were averaged. When only a single observation in a back-and-forth pair was available, this measurement was given half-weight. Analysis of the stellar observations clearly showed that the measurement uncertainty was more accurately reflected by the rms of the individual fluxes about the mean rather than that inferred from the S/N. We developed an empirical model based on the rms of the stellar observations about the DCE mean as functions of focal-plane temperature and irradiance in order to ascribe an un-

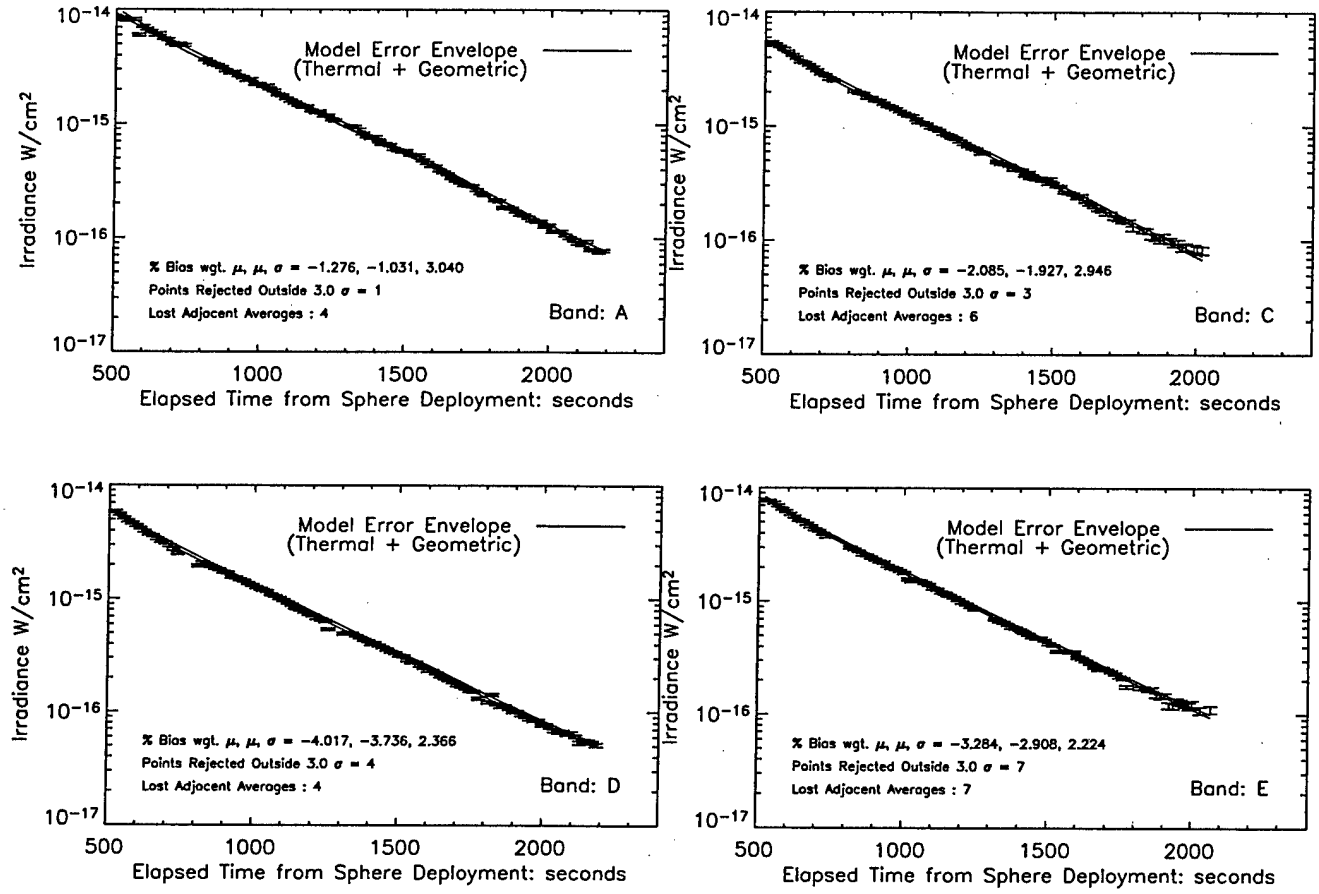

FIG. 8.—*MSX* in-band fluxes for ERS1 plotted as a function of time. The predicted fluxes are plotted as solid lines along with the estimated error in the model. The data points are shown with measurement error bars.

certainty to a single sphere measurement, which is reflected in the measurement error bars plotted in the figure.

It is difficult to visually compare the observations with the model predictions in Figure 8 because of the large dynamic range. The comparison between measurement and model is more clearly seen in Figure 9, in which the biases are plotted as a function of time. The biases are the measurements divided by model predictions minus 1.0. The dashed horizontal line at zero represents the model predictions, the dotted line is the bias (percentage deviation from the model) of the straight average of the measurements, and the dot-dashed line is the weighted average with weights equal to the variance in the error assigned to each measurement. The data are trimmed to reject points greater than 3 σ from the mean. The low signal-to-noise overestimation of the measured flux is apparent at the end of the experiment in bands C, D, and E. We did not attempt to adjust for this bias based on the S/N, such as Tedesco (1994) did to correct the low-S/N *IRAS* photometry of asteroids, because of the uncertain statistical significance of the S/N in the two-tiered measurement extraction criterion. Instead, the inverse-variance weighting of these values, as well as the 3 σ rejection criterion, is used to reduce their contribution to the weighted mean.

A 500 s cyclic variation, most clearly seen in Figure 9 in band D with an 8% peak-to-peak amplitude, is unexplained. Perhaps there is a variation in emissivity over the surface of the sphere that might have been caused by handling or the capture system, although it would be difficult to account for the size of the effect. None of the other spheres were sampled with sufficient density to unambiguously show such a variation.

The weighted average biases for all five spheres and the four mid-infrared spectral bands are listed in Table 5. The next-to-last row of Table 5 lists the weighted average for all five spheres, where the weights are the inverse of the variances about the individual DCE means sum-squared with the model uncertainties in the last paragraph of § 6.5 and the uncertainty is given by equation (5) with $N = 5$, the number of sphere experiments. We also calculated the experiment means in which the weights used were the number of measurements in a DCE divided by the sum squared of the variance in the measurement and model uncertainties. This gives more weight to the more complete and better defined data set from ERS1. These means are listed in the last row of the table. The smaller uncertainties about these means reflect the N-weighting of the DCE measurements in the calculation. The differences between the two sets of means are within 1 σ of the formal solution.

The individual biases in each *MSX* mid-infrared band for each experiment are within the measurement errors. The straight weighted mean in each band averaged over the five experiments is within 2 σ of the uncertainties, while deviations in the N-weighting may be more significant, 4–5 σ, owing to the smaller formal standard deviation in this solution. There is

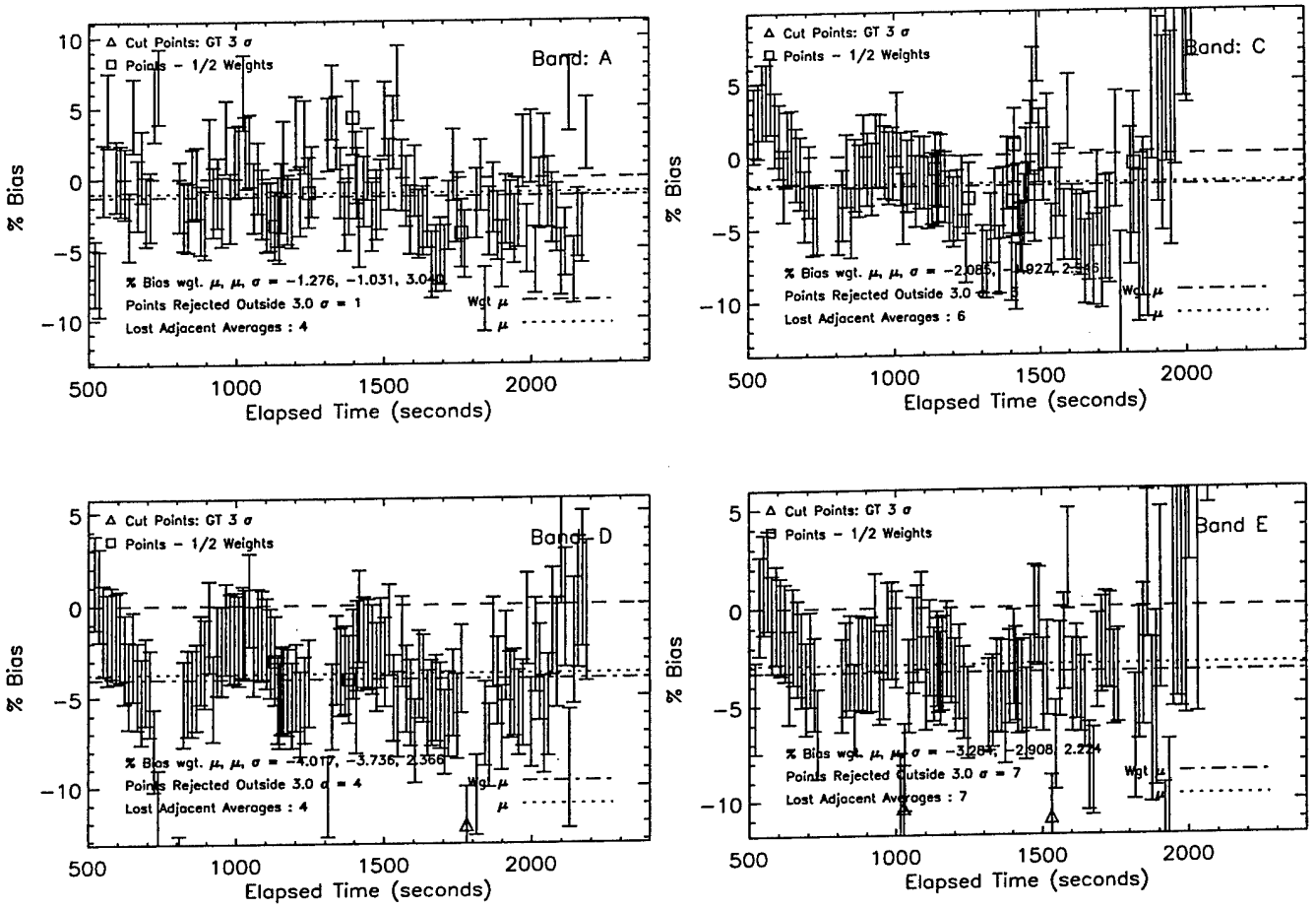

FIG. 9.—Bias of the measurements for ERS1 with respect to the model.

a trend for the mission-averaged biases to decrease with wavelength by about 2.5% from band A to bands D and E, and, among the individual experiments, the trend is most pronounced for ERS2.

The biases measured for the spheres are not entirely random within a DCE, as they are correlated by the fact that the sphere must have a single temperature at the time of observation. Since the range and size of the sphere are the same in all *MSX* bands for a given measurement, the ratio of the flux in two *MSX* bands removes the geometric components and is a measure of the color temperature of the sphere, if the $\leq 1\%$ contribution from the reflected sunlight and earthshine is ignored. The measured band A/C, A/D, A/E, and D/E ratios are compared with the model predictions as a function of time for ERS1 in Figure 10. Only four of the possible six combinations in the ratio are plotted. Bands A, D, and E were purposely co-aligned to facilitate the analysis in these ratios; bands C and D are too close in wavelength to produce a statistically significant ratio, and C/E ratios are consistently noisy. The turnover in the ratios at $t + 1500$ s marks the entry of the sphere into eclipse, at which time the sphere temperature has reached a maximum of 277 K for the DCE. The sphere then cools throughout the eclipse, reaching a minimum of 259 K at the end of the DCE at $t + 2400$ s. Since the other four spheres remain in sunlight during the entire DCE, their temperatures rise to a maximum of 280–282.5 K at the end of the DCE.

The scatter of the DCE biases in the bands about the experiment means may be reduced by adjusting the model

TABLE 5

MEAN PERCENTAGE BIASES AND ERRORS FOR THE ERSs

Experiment	Band A	Band C	Band D	Band E
ERS1	−1.3 ± 3.0	−2.1 ± 2.9	−4.0 ± 2.4	−3.3 ± 2.2
ERS2	3.6 ± 5.1	0.1 ± 2.9	−1.8 ± 2.2	−3.4 ± 3.6
ERS3	2.9 ± 3.8	−2.3 ± 2.6	−2.9 ± 3.2	−2.5 ± 2.4
ERS4	−1.2 ± 3.4	−2.6 ± 3.0	−4.5 ± 4.6	−4.0 ± 1.9
ERS5	−0.8 ± 3.3	−0.2 ± 4.0	−0.7 ± 3.7	0.7 ± 3.5
Weighted mean	0.35 ± 2.0	−1.5 ± 1.1	−2.7 ± 1.3	−2.8 ± 1.5
N-weighted	−0.4 ± 0.7	−1.5 ± 0.4	−2.9 ± 0.6	−2.8 ± 0.7

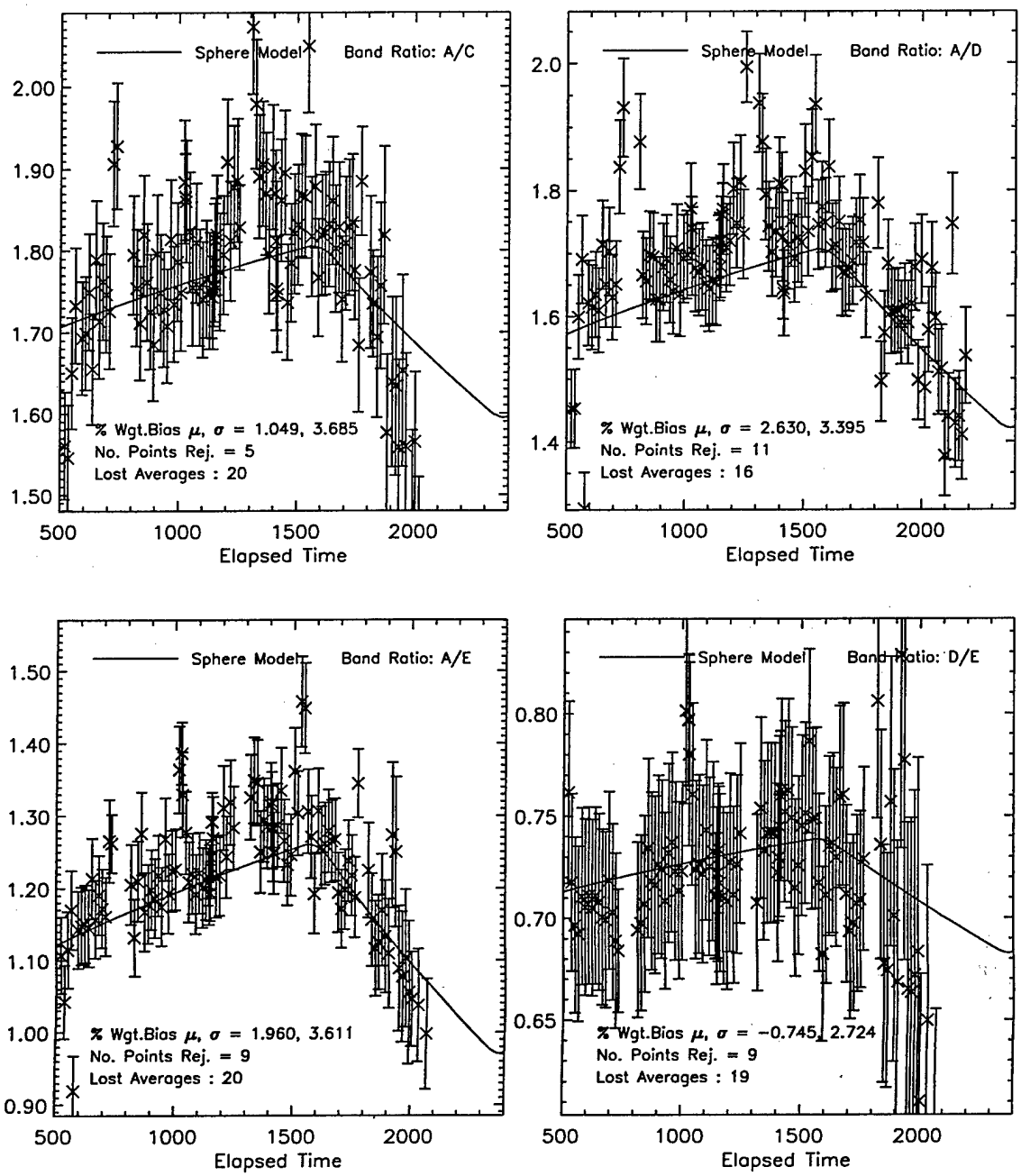

FIG. 10.—Measured compared with modeled band ratios for ERS1.

parameters. The question is, are the required changes within the uncertainties assigned to the parameters? To first order, the biases may be divided into three categories of modeling error: (1) a scaling factor for each band due to errors in the wavelength-dependent emissivity and/or the calibration of the responsivity, (2) geometric factors due to errors in the sphere's radius and/or range, and (3) errors in the thermal model parameters that are manifested as an error in the temperature of the sphere. The band-to-band ratios cancel the geometric factors on a given DCE. Since scaling factors depend on the emissive properties and/or response of the sensor, they should be the same for all five spheres. These two conditions may be used to constrain the solution to the minimum changes in the model to match the observations.

While not strictly correct, we can uncouple the various components in the model by assuming that since the geometric factors cancel in the band ratios and the scale factors are the same for all spheres, the band-to-band ratios averaged over the five experiments are functions only of the scaling factors and the deviations from the means in the band ratios for a given DCE reflect the temperature error. Having defined the average temperature corrections for each DCE, the scale factors and geometric errors are adjusted to match the observed fluxes to the "best" model fit for each DCE in each band. The resulting correlated solution is given in Table 6. The total scatter about the mean scale factors (biases) in Table 6 averaged over the four spectral bands and five DCEs is 0.4% with this solution. The scale factor biases from Table 6

TABLE 6

CORRECTION TO MODEL COMPONENTS FROM BAND RATIOS

Band	Scale Factor Bias	Experiment	Geometric Factor Bias (%)	Temperature Correction (K)
A.....	0.0	ERS1	0.2 ± 0.2	−0.5 ± 0.3
C.....	−1.2	ERS2	−2.5 ± 0.2	3.8 ± 1.1
D.....	−2.9	ERS3	−1.1 ± 1.5	1.6 ± 4.0
E.....	−2.5	ERS4	−1.1 ± 0.1	0.3 ± 0.3
		ERS5	2.9 ± 0.1	−1.9 ± 0.8

and the weighted mean biases from Table 5 agree well within the uncertainties.

There is not enough information to determine how much of the scale factor bias from Table 6 is due to errors in the infrared emissivity of the sphere and how much is the correction to the responsivity. However, the wavelength dependence does mimic that of the infrared emissivity and NIST did measure a mean infrared emissivity that was 1.6% lower than the value derived using the wavelength-dependent emissivities in the model. The geometric factor correction for three of the spheres is within 1 standard deviation of the 1% manufacturing tolerance on the radius of the spheres and the 1% uncertainty in range, and ERS2 and ERS5 are within 2 σ. The trend in the scale factor biases to decrease with wavelength mimics a temperature change of about +2.5 K applicable to all spheres. However, this results in improbably large values of +6.3 K for ERS2. A 1% change in temperature ($\Delta T \sim 2.7$ K) requires a 4% change in the thermal input parameters that define T_{eq} in equation (7). Since the error in the thermal input from the Sun is essentially the 1% uncertainty in the absorptivity, a large change in the flux from Earth is required to change the temperature of the sphere. The flux from Earth constitutes only about ~16% of the thermal input absorbed by the sphere, except for ERS1 while it is in eclipse. A 10% change in thermal input is required to produce a 6.3 K increase in the temperature, which translates into an unlikely 60% increase in flux from Earth. The smaller 3.8 K change required for ERS2 in the solution in Table 6 is also difficult to generate. Except for ERS2, the band ratios for the reference-sphere experiments can be brought into agreement by changing model parameters within 2 σ of the uncertainties of those parameters.

The DC22 reference-sphere experiments also observed the stellar standard stars listed in Table 7. The ratios of the mean fluxes for a star measured on the specified DC22 with the global mean flux in Table 3 are listed. The uncertainty is in the knowledge of the mean in the formal solution, that is, the standard deviation divided by the square root of the number of measurements about the mean for the single DCE, and does not include the additional 1% uncertainty assigned to the DCE means. As may be seen, there are no systematic differences and the ratios are usually within the uncertainty from unity if the additional 1% is included. Statistically, these means may be assumed to belong to the global population of means. This implies that the ERS measurements on the DC22 DCEs are entirely consistent with the stellar calibration observations.

7. ABSOLUTE CALIBRATION OF THE STANDARD STARS

Before drawing conclusions about the absolute stellar flux calibration from the *MSX* measurements, any bias introduced in the stellar analysis must be taken into account. Although the response corrections as a function of focal-plane temperature were normalized to the CWW α CMa fluxes, the mirror-scan DCE mission means for α CMa did not exactly equal those values, because the data for four other calibration stars were included in the derivation of the correction. Scaling the DC-plus-CB averaged mean fluxes such that the averaged results for α CMa were equal to the CWW fluxes further biased the α CMa mirror-scan mission means. The measured fluxes for the reference spheres only applied the temperature-dependent responsivity correction derived from the mirror-scan experiments. Thus, any bias in the DC measurements of α CMa has to be accounted for in order to have the analysis of the reference-sphere observations be compatible with the global stellar solution. Table 8 lists these biases.

The response of the *MSX* mid-infrared bands has been precisely ($\lesssim$0.5% rms) tied to the CWW fluxes for α CMa. Cohen et al. (1992a) based their zero-magnitude fluxes on an absolute flux from α Lyr that was extrapolated into the infrared using a spectral energy distribution of the Kurucz model they selected that was tied to the Hayes (1985) recommended

TABLE 7

FLUX BIASES FOR STARS MEASURED ON THE DC22'S

Observation	Band A	Band C	Band D	Band E
β Peg:				
DC2203.....	1.02 ± 0.02	1.01 ± 0.02	0.924 ± 0.015	1.04 ± 0.03
DC2204.....	0.98 ± 0.02	0.98 ± 0.02	0.995 ± 0.015	1.01 ± 0.03
α Boo:				
DC2201.....	1.006 ± 0.004	1.001 ± 0.004	1.006 ± 0.003	0.995 ± 0.008
α CMa:				
DC2202.....	0.978 ± 0.003	1.006 ± 0.003	0.998 ± 0.003	1.057 ± 0.012
DC2205.....	1.003 ± 0.003	1.007 ± 0.003	1.009 ± 0.003	...
α Lyr:				
DC2201.....	0.998 ± 0.004	1.042 ± 0.011	1.014 ± 0.006	...
DC2202.....	0.999 ± 0.004	1.025 ± 0.011	0.998 ± 0.006	...
α Tau:				
DC2202.....	1.011 ± 0.004	0.990 ± 0.004	0.997 ± 0.003	0.984 ± 0.008
DC2205.....	0.989 ± 0.004	1.001 ± 0.004	1.007 ± 0.003	1.005 ± 0.008
γ Cru:				
DC2201.....	0.995 ± 0.008	0.989 ± 0.007	0.999 ± 0.006	1.002 ± 0.012

TABLE 8

RATIO OF AVERAGED MIRROR-SCAN FLUXES FOR SIRIUS TO THE MISSION MEANS

Band	Ratio
A	1.004 ± 0.003
B_1	1.011 ± 0.007
B_2	1.008 ± 0.006
C	0.998 ± 0.003
D	1.001 ± 0.002
E	1.007 ± 0.030

TABLE 9

CWW ABSOLUTE FLUX BIASES IN THE *MSX* BANDS

Band	Mean Bias (%)
A	0.4 ± 0.7
C	−0.4 ± 0.4
D	−1.9 ± 0.4
E	−2.5 ± 0.6
Mid-IR Avg.	−1.1 ± 0.7

absolute calibration at 0.5556 μm. The *MSX* calibration, however, was normalized to the CWW absolute spectrum of α CMa. To reference the *MSX* calibration to Vega, we divide the measured fluxes in Table 3 for this star by the CWW zero-magnitude fluxes to derive the values listed in Table 4. The high-quality *MSX* Vega measurements in bands A and B_2 average to about 1% lower than the Cohen et al. (1992a) values, as do the global averages for the high-quality observations of the secondary stars in Table 4. Thus, the observations are rationalized by adopting the CWW Vega flux for the zero-magnitude calculations, at least to 12 μm, which brings the average bias of the secondary standards to zero, but at the expense of having to increase the CWW flux for Sirius by 1%. The reference-sphere biases are thus increased by 1%. Table 9 lists our best estimate of the biases derived from the spheres in each *MSX* band from Tables 5 and 6 corrected with the factors in Table 8 and the 1% factor to adjust the stellar analysis to α Lyr. These factors, then, are the biases in the CWW zero-magnitude flux scale derived from the absolute calibration based on the *MSX* reference spheres. The mean bias over the *MSX* bands is −1.1%, well within the 1.45% Cohen et al. (1992a) ascribe to their zero-magnitude flux.

Taking the biases in Table 9 at face value implies that the mid-infrared zero-magnitude fluxes derived by CWW are correct in bands A and C but need to be increased by 2% in band D and 2.5% in band E. Since we cannot separate the uncertainties in the wavelength-dependent emissivities in the model from a calibration error, the best that can be said is that the absolute *MSX* calibration against the emissive reference spheres averaged over the mid-infrared bands is within 1.1% of the CWW zero-point magnitude flux. The *MSX* calibration experiments thus confirm the scale of zero-magnitude fluxes proposed by Cohen et al. (1992a).

8. CONCLUSIONS

The *Midcourse Space Experiment* conducted carefully planned and executed calibration experiments against stellar standards and emissive reference spheres. Almost 200 averaged stellar fluxes were measured on nine of the primary and secondary stars in the CWW calibration network. The formal precision in the knowledge of the mean is a fraction of a percent for the five most frequently measured stars: α CMa, α Tau, α Boo, α Lyr, and β Gem; the sixth star, β Peg, was measured to vary during the mission. Fewer observations were obtained on β And, γ Dra, and γ Cru, and their uncertainties were larger. *MSX* bands D and E observations of α Lyr do not sample purely photospheric radiation but were contaminated by the low-temperature thermal radiation from the circumstellar dust ring around the star; indications are that band C may also be contaminated. Otherwise, the *MSX* observations are within the errors that CWW ascribe to their absolutely calibrated spectra. However, the precision in the *MSX* global means does warrant a reexamination of the CWW spectra. The B-band fluxes for several of the stars are discordant with predictions that are well in excess of the formal errors; β Gem and, perhaps, γ Dra have higher measured fluxes than the CWW calibrated spectra beyond 17 μm. As these stars are used as spectral templates, any error in their CWW spectra is incorporated in the Cohen et al. (1999) network of calibration stars across the sky. However, the *MSX* CB06 analysis confirms the validity of using spectral templates based on composite spectra of the secondary standards for the energy distributions of fainter stars of the same spectral type.

The *MSX* response was absolutely calibrated against five emissive reference spheres whose absolute in-band fluxes were modeled to an accuracy of 3%–4%. The formal measurement accuracy in the weighted average over all *MSX* bands and all experiments is ∼1%. The ERS absolute calibration agrees with the CWW calibration of the spectral energy distribution for a zero-magnitude star to within 1.1%.

MSX was remarkably successful in obtaining an absolute calibration against the reference spheres, given the dynamic operating conditions for the SPIRIT III sensor and the secular changes in response as a function of focal-plane temperature. A more carefully constructed sensor and appropriately planned experiment should produce results with smaller uncertainties.

We thank Martin Cohen and Russ Walker for providing us with the *MSX* in-band fluxes they derived from the absolutely calibrated spectra of the CWW primary and secondary standard stars and for the images from the individual CB06 scan legs, from which we obtained the photometry in this analysis. Beverly Smith very kindly supplied us with the *COBE* DIRBE light curves for the brighter stars observed on the *MSX* calibration experiments. We used the photometric archive of the mirror-scan observations created by Sean Burdick and David Morris, who used the Standard CONVERT routine to extract the fluxes from each scan. Michael Baca, James Elgin, Eric Layton, and Sara-Anne Taylor were the first to recognize the residual variation in the responsivity in the *MSX* bands as a function of focal-plane temperature from the stellar calibration observations. Wes Cobb, Colleen Hamilton, Joseph Howard, and Michael Mavrofrides developed and implemented various routines in the models for the thermal emission from the spheres. We found and corrected errors in the routines that calculated the amount of sunlight reflected by Earth and the thermal emission from Earth that was intercepted by the sphere. Finally, we acknowledge the original *MSX* program manager, Barry Katz (deceased), for his efforts in getting *MSX* flown and placing a high priority on the calibration experiments.

REFERENCES

Abbot, R. I., Gaposchkin, E. M., & von Braun, C. 1997, in Proc. 1997 Space Control Conference, Vol. 2, ed. L. B. Spence (Tech. Rep. ESC-TR-97-063) (Lexington, MA: Lincoln Lab.), 63

Ames, H. O., & Burt, D. A. 1993, Proc. SPIE, 1765, 29

———. 1994, Proc. SPIE, 2227, 74

Bartell, F. O., Hubbs, J. E., Nofziger, M. J., & Wolfe, W. L. 1982, Appl. Opt., 21, 3178

Berk, A., Bernstein, L. S., & Robertson, D. C. 1989, MODTRAN: A Moderate Resolution Model for LOWTRAN 7 (Tech. Rep. GL-TR-89-0122) (Hanscom AFB, MA: Air Force Geophys. Lab.)

Burdick, S. V., & Morris, D. C. 1997, Opt. Eng., 36, 2971

Chalupa, J., Cobb, W. K., & Murdock, T. L. 1991a, Thermal History and Error Budget of an Emissive Calibration Sphere for a Space-based IR Sensor, Part I: Gray-Body Analysis (Tech. Rep. 1597-08-91-TR) (Santa Barbara: Gen. Res. Corp.)

———. 1991b, Proc. SPIE, 1530, 343

Chalupa, J., & Hamilton, C. L. 1993, Thermal History and Error Budget of an Emissive Calibration Sphere for a Space-based IR Sensor, Part II: Spectral Error Analysis (Tech. Rep. 1945-03-93-TR) (Santa Barbara: Gen. Res. Corp.)

Cohen, M., Walker, R. G., Barlow, M. J., & Deacon, J. R. 1992a, AJ, 104, 1650 (erratum 105, 2008 [1993])

Cohen, M., Walker, R. G., Carter, B., Hammersley, P., Kidger, M., & Noguchi, K. 1999, AJ, 117, 1864

Cohen, M., Walker, R. G., Jayaraman, S., Barker, E., & Price, S. D. 2001, AJ, 121, 1180

Cohen, M., Walker, R. G., & Witteborn, F. C. 1992b, AJ, 104, 2030 (erratum 105, 2008 [1993])

Cohen, M., Witteborn, F. C., Carbon, D. F., Davies, J. K., Wooden, D. H., & Bregman, J. D. 1996, AJ, 112, 2274

Cohen, M., Witteborn, F. C., Walker, R. G., Bregman, J. D., & Wooden, D. H. 1995, AJ, 110, 275

de Pater, I., & Lissauer, J. J. 2001, Planetary Sciences (Cambridge: Cambridge Univ. Press)

Egan, M. P., et al. 2003, The *Midcourse Space Experiment* Point Source Catalog Version 2.3 Explanatory Guide (Tech. Rep. AFRL-TR-2003-1589) (Hanscom AFB, MA: Air Force Res. Lab.)

Engelke, C. W. 1992, AJ, 104, 1248

Garlick, D. S., Greenman, M., Larsen, M. F., Sargent, S., & Hanson, J. S. 1996, Proc. SPIE, 2759, 182

Hayes, D. S. 1985, in IAU Symp. 111, Calibration of Fundamental Stellar Quantities, ed. D. S. Hayes, L. E. Pasinetti, & A. G. D. Philip (Dordrecht: Reidel), 225

Heinrichsen, I., Walker, H. J., & Klaas, U. 1998, MNRAS, 293, L78

Hodgman, C. D., Weast, R. C., & Selby, S. M., eds. 1957, Handbook of Chemistry and Physics (39th ed.; Cleveland: Chem. Rubber Pub.)

Kintner, E. C., & Sohn, R. B. 1993a, Thermal Modeling of *MSX* Spacecraft Emissive Reference Spheres for LWIR Sensor Calibration (Project Rep. SDP-368) (Lexington, MA: Lincoln Lab.)

———. 1993b, Proc. SPIE, 1938, 153

Kittel, C. 1986, Introduction to Solid State Physics (6th ed.; New York: Wiley)

Larsen, M. F., & Sargent, S. D. 1997, Opt. Eng., 36, 2956

Larsen, M. F., Sargent, S. D., & Tansock, J. J., Jr. 1998a, Proc. SPIE, 3373, 32

Larsen, M. F., Tansock, J. J., Jr., Sorenson, G. O., Garlick, D. S., & Hansen, J. S. 1996, Proc. SPIE, 2759, 194

Larsen, M. F., Thurgood, V. A., & Sargent, S. D. 1998b, in Proc. Eighth SDL/USU Symp. on Infrared Radiometric Sensor Calibration (Logan, UT: Space Dyn. Lab., Utah State Univ.)

Marquardt, E. D., Le, J. P., & Radebaugh, R. 2001, in Cryocoolers 11, ed. R. G. Ross, Jr. (New York: Plenum), 681

Mavrofrides, M. A., Burdick, S. B., Murdock, T., & Pollack, D. 1998, in Proc. Eighth SDL/USU Symp. on Infrared Radiometric Sensor Calibration (Logan, UT: Space Dyn. Lab., Utah State Univ.)

Mazuk, S., & Lillo, W. 1998, in Proc. Eighth SDL/USU Symp. on Infrared Radiometric Sensor Calibration (Logan, UT: Space Dyn. Lab., Utah State Univ.)

Mill, J. D., et al. 1994, J. Spacecr. Rockets, 31, 900

National Institute of Standards and Technology. 1993, Absolute Broadband LWIR Radiant Flux Measurements of Martin Black Samples of Simulated Reference Spheres for the *MSX* Program (Meas. 844/LBIR-7-93; TP-010700-001-F01.00-930909) (Gaithersburg, MD: NIST)

Pompea, S. M., Bergener, D. W., Shepard, D. F., Russak, S., & Wolfe, W. L. 1984, Opt. Eng., 23, 149

Price, S. D., Egan, M. P., Carey, S. J., Mizuno, D. R., & Kuchar, T. A. 2001, AJ, 121, 2819

Sargent, S. D. 1997, Opt. Eng., 36, 2948

Schatten, K. H., & Orosz, J. 1990, Sol. Phys., 125, 179

Smith, B. J. 2003, AJ, 126, 935

Surface Optics Corporation. 1993, Directional Reflectance Measurements on Seven MIT/LL Supplied Sample Materials (Tech. Rep. SOC-R761-001-0493) (San Diego: Surface Opt. Corp.)

Tedesco, E. F. 1994, in IAU Symp. 160, Asteroids, Comets, Meteors 1993, ed. A. Milani, M. Di Martino, & A Cellino (Dordrecht: Kluwer), 55

Thurgood, V. A., Larsen, M. F., & Sargent, S. D. 1998, in Proc. Eighth SDL/USU Symp. on Infrared Radiometric Sensor Calibration (Logan, UT: Space Dyn. Lab., Utah State Univ.)

Tobiska, W. K. 2002, Adv. Space Res., 29, 1969

Wilson, C. F. 1992, in Proc. Third SDL/USU Symp. on Infrared Radiometric Sensor Calibration (Logan, UT: Space Dyn. Lab., Utah State Univ.)